Article

Two-Band Superconductivity and Transition Temperature Limited by Thermal Fluctuations in Ambient Pressure $La_{3-x}Pr_xNi_2O_{7-\delta}$ (x = 0.0, 0.15, 1.0) Thin Films

Evgeny Talantsev [*]

Article

Two-Band Superconductivity and Transition Temperature Limited by Thermal Fluctuations in Ambient Pressure La₃-ₓPrₓNi₂O₇-δ (x = 0.0, 0.15, 1.0) Thin Films

Evgeny F. Talantsev [1,2,*]

[1]   M.N. Miheev Institute of Metal Physics, Ural Branch, Russian Academy of Sciences, 18, S. Kovalevskoy St., Ekaterinburg, 620108, Russia; evgeny.talantsev@imp.uran.ru

[2]   NANOTECH Centre, Ural Federal University, 19 Mira St., Ekaterinburg, 620002, Russia

Abstract: Recently, two research groups[1–3] reported on the observation of ambient pressure superconductivity in a few nanometres thick La₃-ₓPrₓNi₂O₇-δ (x = 0.0, 0.15, 1.0) films with the $T_{c,onset} \cong 40\,K$ and $T_{c,zero} \leq 14\,K$. Here I have analysed the reported self-field critical current density, $J_c(sf,T)$, and upper critical field, $B_{c2}(T)$, for these films[1–3] and showed that La₃-ₓPrₓNi₂O₇-δ films exhibit a large in-plane London penetration depth, $\lambda_{ab}(0) = 1.9 - 6.8\,\mu m$, and the Ginzburg-Landau parameter $\kappa_c(0) = 500 - 1000$. Deduced $\lambda_{ab}(0)$ values are within uncertainty range for independently reported[2] $\lambda_{ab}(T = 1.8\,K) = 3.7\pm^{1.4}_{1.9}\,\mu m$. Such large $\lambda_{ab}(0)$ implies that the La₃-ₓPrₓNi₂O₇-δ exhibits low ground state lower critical field $B_{c1}(0) = (20 - 240)\,\mu T$. On the other hand, such large values of $\lambda_{ab}(0)$ explain the broad resistive transition in La₃-ₓPrₓNi₂O₇-δ films[1–3], because large $\lambda_{ab}(0)$ implies low superfluid density, $\rho_s \equiv \frac{1}{\lambda_{ab}^2}$, and therefore large thermal fluctuations. Consequently, I calculated the phase fluctuation temperature, T_{fluc}, and found that the $T_{c,zero} < T_{fluc}$. I also found that $J_c(sf,T)$ and $B_{c2}(T)$ data are nicely fitted to two-band models, from which the preference has been given to two-band (*s+s*)-wave model (for which the ratios of $\frac{2\Delta_L(0)}{k_B T_{c,L}} \cong 3.6 - 4.0$ and $\frac{2\Delta_S(0)}{k_B T_{c,S}} = 1.0 - 3.0$ for the larger and smaller bands have been deduced, respectively). Besides I showed that bulk highly compressed Ruddlesden–Popper nickelates Laₙ₊₁NiₙO₃ₙ₊₁ (*n* = 2,3) and ambient pressure Laₙ₊₁NiₙO₂ₙ₊₂ (*n* = 5) thin film also demonstrate evidences for two-band superconductivity.

Keywords: superconducting nickelates; self-field critical current; upper critical field; two-band superconductivity

I. Introduction

High-temperature superconductivity in nickelates had predicted by first principles calculations[4] in 1999 and experimentally discovered in several nanometers thick Nd₁-ₓSrₓNiO₂ films[5] twenty years later. Recently, high-temperature superconductivity in highly compressed bulk nickelate phase La₃Ni₂O₇-δ (LNO-327) has been reported[6]. Despite a fact that this phase had been synthesized more than four decades ago[7], and it had been intensively studied[8–11] since then (including studies at high pressure[12]), only experiments at pressures above 10 GPa allowed to detect the high-temperature superconductivity in bulk La₃Ni₂O₇-δ samples. Very recently two research groups[1,2] reported on the observation of ambient pressure superconducting state with $T_{c,onset} \cong 40\,K$ and $T_{c,zero} = 2 - 9\,K$ in a few nanometers thick epitaxial La₃-ₓPrₓNi₂O₇-δ (x = 0.0, 0.15) films. It should be noted that nearly two decades ago[13], epitaxial Laₙ₊₁NiₙO₃ₙ₊₁ (n = 1,2,3,∞) films with thickness 130-200 nm had been fabricated and studied; however, temperature dependent resistivity $\rho(T)$ in these films was measured in the range of $300\,K \lesssim T \lesssim 900\,K$[13] only.

Here from an analysis of temperature dependent self-field critical current density, $J_c(sf, T)$, reported for La$_{3-x}$Pr$_x$Ni$_2$O$_{7-\delta}$ (x = 0.0, 0.15, 1.0) films[1–3] we extracted the ground state in-plane London penetration depth, $\lambda_{ab}(0)$, the Ginzburg-Landau parameter, $\kappa_c(0)$, BCS ratios (the gap-to-transition temperature ratio, $\frac{2\Delta(0)}{k_B T_c}$, and relative jump in electronic specific heat at the transition temperature, $\frac{\Delta C_{el}}{\gamma T_c}$), and explained a large width of the resistive transition as manifestation of low superfluid density in these films. We also found that two-band *s*-wave superconductivity is a preferable model for the order parameter in the La$_{3-x}$Pr$_x$Ni$_2$O$_{7-\delta}$ (x = 0.0, 0.15, 1.0) films[1–3] for existing experimental $J_c(sf, T)$ data.

II. Fundamental Parameters for La$_{3-x}$Pr$_x$Ni$_2$O$_{7-\delta}$ (x = 0.0; 0.15; 1.0) Films

2.1. Transition Temperature and Coherence Length Definitions

Superconducting coherence length, $\xi(T)$, is one of two fundamental lengths of any superconductor. Commonly accepted simple approach to determine the ground state coherence length, $\xi(0)$, is to fit the upper critical field data, $B_{c2}(T)$, to the Ginzburg-Landau expression:

$$B_{c2}(T) = \frac{\phi_0}{2\pi \xi^2(T)} \tag{1}$$

where $\phi_0 = \frac{h}{2e}$ is the superconducting flux quantum, h is the Planck's constant, e is the electron charge. From several available analytical approximations of Eq. 1 within frames of the Werthamer-Helfand-Hohenberg (WHH) theory[14,15], here we used two expressions[16,17]:

$$B_{c2,c}(T) = \frac{1}{0.693} \times \frac{\phi_0}{2\pi \xi_{ab}^2(0)} \times \left(\left(1 - \frac{T}{T_c}\right) - 0.153 \times \left(1 - \frac{T}{T_c}\right)^2 - 0.152 \times \left(1 - \frac{T}{T_c}\right)^4 \right), \tag{2}$$

$$B_{c2,c}(T) = \frac{\phi_0}{2\pi \xi_{ab}^2(0)} \times \left(\frac{1 - \left(\frac{T}{T_c}\right)^2}{1 + 0.42 \times \left(\frac{T}{T_c}\right)^{1.47}} \right), \tag{3}$$

where $B_{c2,c}(T)$ is the out-of-plane upper critical field, $\xi_{ab}(0)$ is the ground state in-plane coherence length, and $\xi_{ab}(0)$ and T_c are free fitting parameters. Eq. 2 will be designated as B-WHH model[16], and Eq.3 will be designated as PK-WHH[17] model below. From our experience, data fits to Eqs. 2,3 results in very close $\xi(0)$ and T_c values (but for the purpose of verification of the deduced free fitting parameters we used both fits).

The crucial issue here is the criterion of the upper critical field definition, $B_{c2}(T)$, which can be applied to available experimental data. Theoreticians rarely discuss this key issue, and experimentalists tend to overestimate (sometimes by manifold) the $B_{c2}(T)$ values by chosen high resistive criteria[1,2,5,6,18–22]:

$$\frac{R(T=T_{c,0.50})}{R(T=T_{c,onset})} = 0.50 \tag{4}$$

where $R(T = T_{c,onset})$ is the resistance at temperature, where $R(T)$ starts to drop.

It should be also noted that several research groups[22,23] demonstrated the consequences of applying different resistive criteria, $\frac{R(T=T_c)}{R(T=T_{c,onset})}$, for the $B_{c2}(T)$ definition for infinite-layer nickelate superconductor Nd$_{1-x}$Sr$_x$NiO$_2$. For instance, Wang *et al*[22] showed that applying different criteria for $R(T)$ data for Nd$_{0.775}$Sr$_{0.225}$NiO$_2$ film results in manifold difference in the $B_{c2}(T)$ values (and at some temperatures, the difference is more than 20 times). Moreover, different criteria result in different shapes of the temperature dependent $B_{c2}(T)$. Because the $B_{c2}(T)$ shape is a primary property which is analyzed by the WHH theory[14,15], this implies that fundamental superconducting parameters deduced by this theory[14,15] depend not from fundamental intrinsic properties of the superconductor, but they determined by the chosen criterion for the upper critical field definition.

In regard of highly compressed La₃Ni₂O₇ phase, the large difference between extrapolated ground state upper critical field value $B_{c2}(0)$ when different resistive criteria was applied has been demonstrated by Zhang *et al.*[24].

These issues demonstrate a large uncertainty associated with the one of two fundamental fields of any type-II superconductor, which is unusual for any fundamental property of material.

To resolve this issue, from our view, the criterion should be as strict as it is practically possible:

$$\frac{R(T=T_{c,zero})}{R(T=T_{c,onset})} \to 0 \tag{5}$$

because the superconducting state has several unique properties, and one of them is the entire zero resistivity. And because of this, it is incorrect to designate the superconducting coherence length to the state at which the material[25–27] (including, nickelates[1,2,5,18,21,28–30]) exhibits the resistivity of:

$$\rho(T \cong 15\,K) = (3-10) \times 10^{-5}\,\Omega \times \text{cm} \tag{6}$$

which is the respective resistivity value to Eq. 4. The level of resistivity described by Eq. 6 is by several orders of magnitude exceeds the resistivity of noble normal metals at the same temperatures. In term of resistance, Eqs. 4,6 often imply that the T_c is defined[25–27] at $R(T = T_{c,0.50}) \cong 5,000\,\Omega$, which cannot be accepted to be the resistance of the superconducting state by any standards.

It should be stressed that initial drop in resistance at $T_{c,onset}$ originates from thermodynamic fluctuations[22,31–33] *"occurring at temperatures above the superconducting transition temperature"*[34], which is $T_{c,zero}$. The strength of these fluctuations can be quantified by two characteristic temperatures, which we calculated for the La₃₋ₓPrₓNi₂O₇₋δ (x = 0.0, 0.15, 1.0) films below (see Section 4).

Despite strict criterion (Eq. 5) is in a rare use, there are several research groups who implemented this criterion to define the T_c and $B_{c2}(T)$[24,35–48]. It should be noted that there are several other strict criteria for the T_c and $B_{c2}(T)$ definitions (for instance, these criteria are based on the onset of the diamagnetic response[40,49–55], the peak of the jump in the specific electronic heat[56–62], or on the onset of the spontaneous Nernst effect[48], or superconducting gap closing[63]). Some research groups use several techniques and criteria[48,64–69] to define the T_c and $B_{c2}(T)$.

However, the majority of reports on thin film superconductors utilize the manifold overestimated criterion (Eq. 4)[1–3,5,21,25,26,30,70,71]. In a particular case of the La₃Ni₂O₇₋δ films[1], the difference between $T_{c,0.90} = 38\,K$ and $T_{c,zero} \cong 3\,K$ (see Figures 1,3 in Ref.[1]) is remarkable. Based on that, the difference between the $B_{c2,c}(T)$ and $\xi_{ab}(0)$ defined by different criteria are enormous. Similar problem is for La₂.₈₅Pr₀.₁₅Ni₂O₇₋δ films[2], for which the $T_{c,0.90} = 32\,K$ and $T_{c,zero} \cong 9\,K$ (see Figures 2 in Ref.[2]).

Additional reason for defining the transition temperature by Eq. 5 is the request to harmonize parameters of another genuine phenomenon of superconductors, which is dissipative-free electric current flow. The current becomes dissipative at some value, known as critical current, I_c, and material resistivity at this state[72] is:

$$\rho(I = I_c) = 10^{-13}\,\Omega \times \text{cm}, \tag{7}$$

which is by eight-nine orders of magnitude lower than the half of normal state resistivity in nickelate films[1–3,5,18,21,28–30] (Eq. 4).

Considering that the critical current density (which is $J_c = \frac{I_c}{A}$, where A is cross-section of the conductor) in the absence of external magnetic field, which is designated as the self-field critical current density, $J_c(sf,T)$, in thin-film superconductors describes by universal equation[73]:

$$J_c(sf,T) = \frac{\phi_0}{4\pi\mu_0} \frac{ln\left(\frac{\lambda_{ab}(T)}{\xi_{ab}(T)}\right)+0.5}{\lambda_{ab}^3(T)} \tag{8}$$

where $\mu_0 = 4\pi10^{-7}\,\frac{N}{A^2}$ is the permeability of free space, and $\lambda_{ab}(T)$ is London penetration depth, there is a request that $\lambda_{ab}(T)$ and $\xi_{ab}(T)$ should be harmonized.

Otherwise, if $\xi_{ab}(T)$ will be defined by Eq. 4, and $\lambda_{ab}(T)$ will be defined by Eq. 7, then the Ginzburg-Landau parameter, $\kappa_c(T) = \frac{\lambda_{ab}(T)}{\xi_{ab}(T)}$, and the lower critical field:

$$B_{c1}(T) = \frac{\phi_0}{4\pi} \frac{ln(\kappa_c(T))+0.5}{\lambda_{ab}^2(T)},$$
(9)

would be undefined for a large temperature range between $T_{c,0.90} = 38\ K$ and $T_{c,zero} = 3\ K$ (see Figures 1,3 in Ref.[1]).

This implies that T_c should be defined by a condition at which both characteristic lengths, $\lambda_{ab}(T)$ and $\xi_{ab}(T)$, as well as, other related fundamental parameters, do exist:

$$\begin{cases} \lambda(T \to T_c) \to \infty \\ \xi(T \to T_c) \to \infty \\ \kappa \ni (T \leq T_c) \\ J_c(sf, T = T_c) = 0 \\ B_{c1}(T = T_c) = 0 \\ B_{c2}(T = T_c) = 0 \end{cases}$$
(10)

For instance, the La₃Ni₂O₇₋δ film[1] exhibits (Figure 3,a[1], insert):

$$J_c(sf, T \to 3\ K) \to 0$$
(11)

and this implies that:

$$\begin{cases} \lambda_{ab}(T \to 3.0\ K) \to \infty \\ \xi_{ab}(T \to 3.0\ K) \to \infty \\ T_c = 3.0\ K \end{cases}$$
(12)

All $J_c(sf, T)$ data fits were performed with homemade software freely available online[74].

2.2. London Penetration Depth and Other Fundamental Parameters

There are two available $R(T,B)$ datasets for the La₃Ni₂O₇₋δ films reported by Ko *et al*[1], for which we applied the resistive criteria discussed above:

1. For Figure 3,b[1]:

$$\frac{\rho(T=T_c)}{\rho(T=T_{c,onset})} = \frac{\rho(T=T_c=3.5\ K)}{\rho(T=40\ K)} \cong \frac{0.014\ m\Omega \times cm}{0.23\ m\Omega \times cm} = 0.06$$
(13)

2. For the Extended Data Figure 3,a[1]:

$$\frac{R(T=T_c)}{R(T=T_{c,onset})} = \frac{R(T=T_c=3\ K)}{R(T=10\ K)} \cong \frac{6\ \Omega}{30\ \Omega} = 0.2$$
(14)

Despite both $R(T,B)$ datasets (i.e. Figure 3,b[1] and Extended Data Figure 3,a[1]) consists of only two curves which satisfy the condition (Eqs. 13,14), it is still possible to estimate the $\xi_{ab}(0)$ value in the La₃Ni₂O₇₋δ films[1], from the data fits to Eqs. 2,3 (Figure 1).
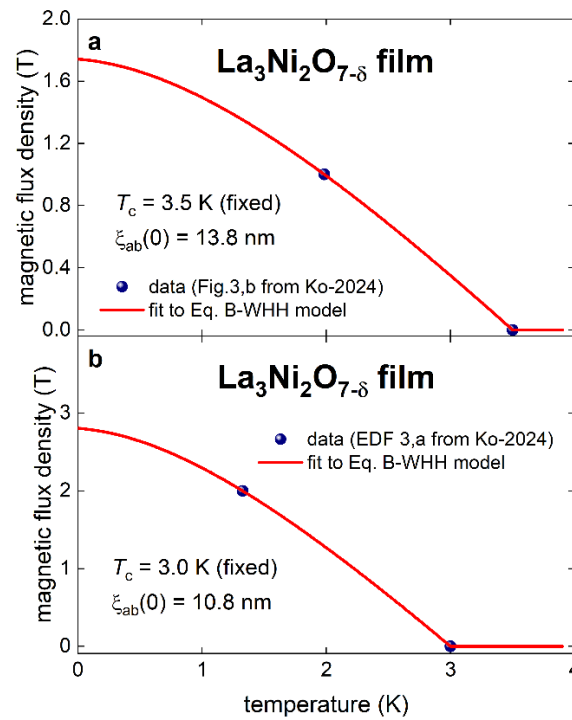
Figure 1. Estimated values for $\xi_{ab}(0)$ for the ambient pressure La₃Ni₂O₇₋δ films[1].   (**a**) $R(T,B)$ data from Figure 3,b[1] by applying criterion described by Eq. 8 and data fit to Eq. 2; (**b**) $R(T,B)$ data from Extended Data and Figures 3,a[1] by applying criterion described by Eq. 9 and data fit to Eq. 3.

As a result, we estimated the ground state coherence length in the La₃Ni₂O₇₋δ films[1] as the average value of:

$$\xi_{ab}(0) = 12 \, nm \tag{15}$$

However, detailed experimental $R(T,B)$ data in the temperature range of $0 < T \leq 4\,K$ and field range of $0 \leq B \leq 3\,T$ range is required to determine the $\xi_{ab}(0)$ value more accurately.

Because the self-field critical current density, $J_c(sf,T)$, has a very weak dependence (Eq. 6) from temperature dependent Ginsburg-Landau parameter, $\kappa_c(T) = \frac{\lambda_{ab}(T)}{\xi_{ab}(T)}$, we simplify Eq. 6 to the form[73]:

$$J_c(sf,T) = \frac{\phi_0}{4\pi\mu_0} \frac{ln\left(\frac{\lambda_{ab}(0)}{\xi_{ab}(0)}\right) + 0.5}{\lambda_{ab}^3(T)} \tag{16}$$

where $\xi_{ab}(0) = 12\,nm$ (Eq. 12) is fixed parameter.

Temperature dependent London penetration depth for *s*-wave superconductors is given by the following equation[75,76]:

$$\lambda_{ab}(T) = \frac{\lambda_{ab}(0)}{\sqrt{1 - \frac{1}{2k_BT} \times \int_0^\infty \frac{d\varepsilon}{\cosh^2\left(\frac{\sqrt{\varepsilon^2 + \Delta^2(T)}}{2k_BT}\right)}}} \tag{17}$$

where k_B is the Boltzmann constant. Temperature dependent superconducting gap amplitude, $\Delta(T)$, can be described by analytical expression[75,76]:

$$\Delta(T) = \Delta(0) \times tanh\left[\frac{\pi k_B T_c}{\Delta(0)} \times \sqrt{\eta \times \frac{\Delta C_{el}}{\gamma T_c} \times \left(\frac{T_c}{T} - 1\right)}\right] \tag{18}$$

where $\eta \equiv \frac{2}{3}$ for *s*-wave superconductors[75,76], and $\frac{\Delta C_{el}}{\gamma T_c}$ is the relative jump in the electronic heat at T_c, and γ is the Sommerfeld parameter. Direct measurements of superconducting gap in highly compressed elemental sulfur[63] confirmed temperature dependent shape of the $\Delta(T)$ described by Eq. 18.

For *d*-wave superconductors, London penetration depth is given by[75,76]:

$$\lambda_{ab}(T) = \frac{\lambda_{ab}(0)}{\sqrt{1 - \frac{1}{2\pi k_B T} \times \int_0^{2\pi} cos^2(\theta) \times \left(\int_0^\infty \frac{d\varepsilon}{cosh^2\left(\frac{\sqrt{\varepsilon^2 + \Delta^2(T,\theta)}}{2k_B T} \right)} \right) d\theta}} \tag{19}$$

where the superconducting energy gap, $\Delta(T, \theta)$, is given by[75,76]:

$$\Delta(T, \theta) = \Delta_m(T) \times cos(2\theta) \tag{20}$$

where $\Delta_m(T)$ is the maximum amplitude of the *k*-dependent *d*-wave gap given by Eq. 15, θ is the angle around the Fermi surface subtended at (π, π) in the Brillouin zone (details can be found elsewhere[75,76]), and $\eta \equiv \frac{7}{5}$ in accordance with Refs.[75–78].

p-wave superconductors have the gap function given by[75,76,79]: $\Delta(\vec{k}, \vec{l}, T) = \Delta(T) \times f(\vec{k}, \vec{l})$ (21)

where Δ is the superconducting gap, $\vec{k}$ is the wave vector, and $\vec{l}$ is the gap axis. The electromagnetic response depends[80] on the mutual orientation of the vector potential $\vec{A}$ and the gap axis $\vec{l}$. At experimental conditions during the self-field critical current measurements in epitaxial thin films this is the orientation of the crystallographic axes compared with the direction of the electric current[80]. In addition, from four different *p*-wave pairing states (which are two "axial" states, where there are two point nodes, and two "polar" states, where there is an equatorial line node), previous analysis[80] showed that the only *p*-wave case that is distinguishable from dirty *s*- and *d*-wave is the *p*-wave polar $\vec{A} \perp \vec{l}$ case. Details can be found in Ref.[80]. For this polar $\vec{A} \perp \vec{l}$ *p*-wave case the London penetration depth is given by[75,76,80]:

$$\lambda_{ab}(T) = \frac{\lambda_{ab}(0)}{\sqrt{1 - \frac{3}{4k_B T} \times \int_0^1 \frac{(1-x^2)}{2} \times \left(\int_0^\infty \frac{d\varepsilon}{cosh^2\left(\frac{\sqrt{\varepsilon^2 + \Delta^2(T) \times f^2(x)}}{2k_B T} \right)} \right) dx}} \tag{22}$$

where the superconducting energy gap, is given by Eq. 21, where[75,76,80]:

$$\Delta(T) = \Delta(0) \times tanh\left[\frac{\pi k_B T_c}{\Delta(0)} \times \sqrt{\eta \times \frac{\Delta C_{el}}{\gamma T_c} \times \left(\frac{T_c}{T} - 1 \right)} \right] \tag{23}$$

$$\eta = \frac{2}{3} \frac{1}{\int_0^1 f^2(x) dx} \tag{24}$$

$$f(x) = x \tag{25}$$

Ko *et al*[1] reported the $J_c(sf, T)$ data for the La₃Ni₂O₇₋δ film in Figure 3,a[1], which we fitted to single *s*-, *d*-, and polar $\vec{A} \perp \vec{l}$ *p*-wave gap symmetry models (Eqs. 16-25) in Figure 2.
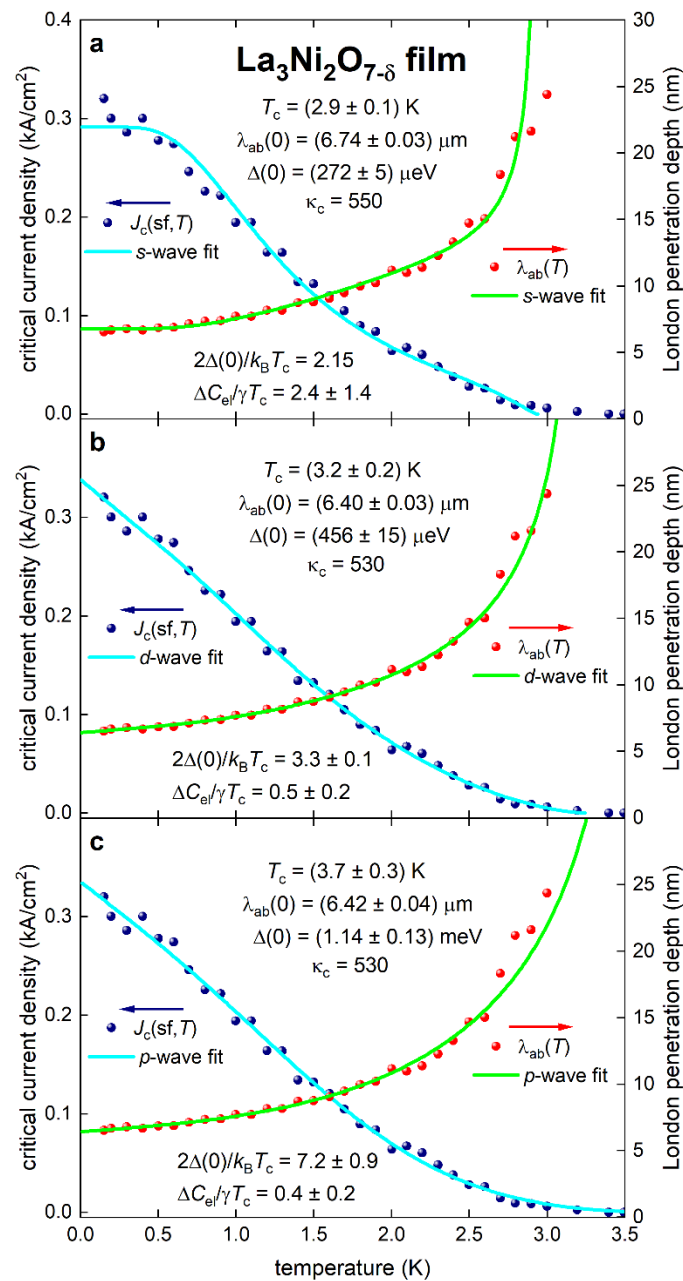
Figure 2. The self-field critical current density, $J_c(sf, T)$, for the ambient pressure La₃Ni₂O₇₋δ film[1] (reported by Ko *et al*[1] in their Figure 3,a[1]) and data fit to the single band model (Eq. 16) with symmetry of (**a**) *s*-wave (Eqs. 17,18, fit quality $R = 0.9575$); (**b**) *d*-wave (Eqs. 18-20, fit quality $R = 0.9810$); and (**c**) polar $\vec{A} \perp \vec{l}$ *p*-wave (Eqs. 22-25, fit quality $R = 0.9849$). Derived parameters are shown in each panel. $\xi_{ab}(0) = 12\ nm$ was assumed for all fits.

Deduced unitless BCS ratios (Figure 2) are in large difference from the weak-coupling limits for *s*-, *d*-, and polar $\vec{A} \perp \vec{l}$ *p*-wave symmetries[75–77,80–82]:

$$\frac{2\Delta(0)}{k_B T_c} = 3.53; \quad \frac{\Delta C_{el}}{\gamma T_c} = 1.43 \quad \text{(weak-coupling limits for } s\text{-wave symmetry)} \tag{26}$$

$$\frac{2\Delta_m(0)}{k_B T_c} = 4.28; \quad \frac{\Delta C_{el}}{\gamma T_c} = 0.995 \quad \text{(weak-coupling limit for } d\text{-wave symmetry)} \tag{27}$$

$$\frac{2\Delta_m(0)}{k_B T_c} = 4.92; \quad \frac{\Delta C_{el}}{\gamma T_c} = 0.792 \quad \text{(weak-coupling limit for polar } \vec{A} \perp \vec{l}\ p\text{-wave symmetry)} \tag{28}$$

Thus, we concluded that ambient pressure La₃Ni₂O₇₋δ films are multiple-band superconductor.

2.3. Two-Band Superconductivity

Thus, we tested six possible two-band cases (i.e. *s-* + *s-*; *s-* + *d-*; …, *p-* + *p-*) of superconductivity in these films. To do this, we used two-band model[77,83]:

$$J_{c,total}(sf,T) = J_{c,band1}(sf,T) + J_{c,band2}(sf,T) \tag{29}$$

where $band1$ and $band2$ designate critical current density originated from respectful band; each band has its independent $\Delta_i(0)$, $\lambda_{ab,i}(0)$, $\left(\frac{\Delta C_{el}}{\gamma T_c}\right)_i$, and $T_{c,i}$ (Eqs. 16-25). We used fixed $\xi_{ab}(0) = 12\ nm$ value for both bands.

From performed fits of the $J_c(sf,T)$ data to six possible two-band models, we found that deduced parameters for two-band *s*-wave model are in reasonable proximity to the values reported for MgB$_2$ superconductor[84–86] (Figure 3). It should be noted, that in this fit we assumed the condition[77,83] of:

$$\left(\frac{\Delta C_{el}}{\gamma T_c}\right)_{band1} = \left(\frac{\Delta C_{el}}{\gamma T_c}\right)_{band2} \tag{30}$$

by keeping this joint parameter to be free. Without this restriction, several deduced parameters have large uncertainties. Denser raw $J_c(sf,T)$ dataset with measurements performed with a smaller temperature step ($\Delta T \cong \frac{T_c}{200}$) would make it possible to deduce separate values for $\left(\frac{\Delta C_{el}}{\gamma T_c}\right)$ for each band.
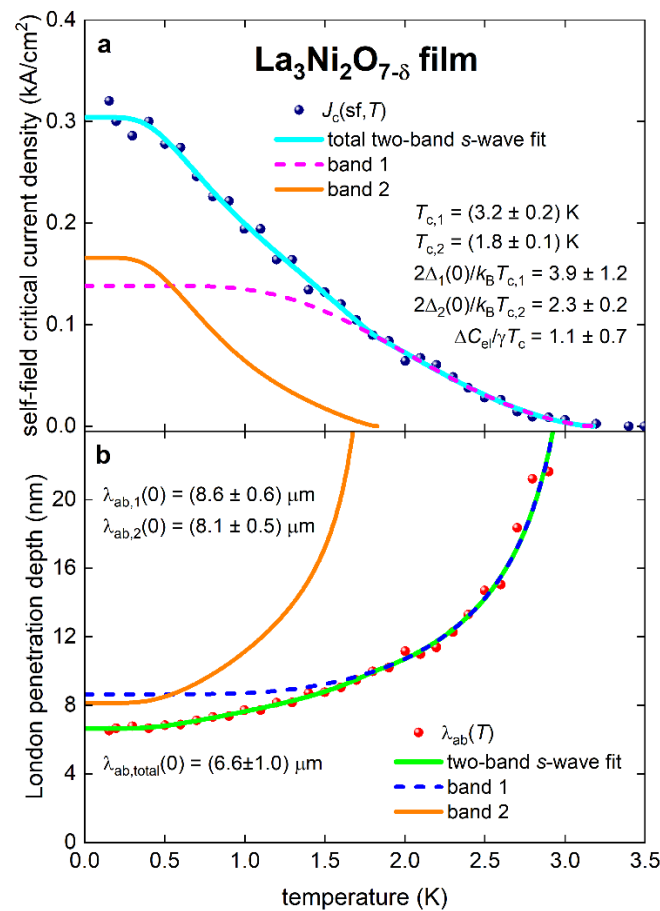

Figure 3. The self-field critical current density, $J_c(sf,T)$, for the ambient pressure La$_3$Ni$_2$O$_{7-\delta}$ film[1] (reported by Ko *et al*[1] in their Figure 3,a[1]) and data fit to two-band (*s-* + *s-*)-wave model (Eq. 29). The restriction of $\left(\frac{\Delta C_{el}}{\gamma T_c}\right)_{band1} = \left(\frac{\Delta C_{el}}{\gamma T_c}\right)_{band2}$ has been implemented. Fit quality is $R = 0.9674$. Derived parameters are shown. $\xi_{ab}(0) = 12\ nm$ was assumed. (**a**) data and fitting curves are shown for $J_c(sf,T)$ data; (**b**) data and fitting curves are shown for $\lambda_{ab}(T)$ data.

Fits to other two-band models (Eq. 29) are either diverged, either the deduced parameters are in times different from respectful weak coupling limiting values (Eqs. 26-28). Fits to three-band models are possible in principle, but to do this, the experimental $J_c(sf,T)$ dataset should be very dense with $\Delta T \cong \frac{T_c}{1000}$ and covers as lower as possible temperature range.

It should be stressed that independent from assumed pairing symmetry and/or multiple-band superconductivity, the absolute values of $\lambda_{ab}(0) \cong 6.5\ \mu m$ and $\kappa_c(0) \cong 550$ are remaining the same. The former value is in close proximity to the $\lambda_{ab}(0, P = 16.6\ GPa) \cong 6.0\ \mu m$ determined[87] from the $J_c(sf,T)$ data reported for highly compressed bulk La₃Ni₂O₇₋δ sample[24]. Both these $\lambda_{ab}(0)$ values are in the same ballpark with the upper limit of $\lambda_{ab}(T = 1.8\ K) = 3.7\pm^{1.4}_{1.9}\ \mu m$ recently reported for La₂.₈₅Pr₀.₁₅Ni₂O₇₋δ thin film by independent research group[2].

III. Fundamental Parameters in La₂PrNi₂O₇₋δ Films

To deduce in-plane ground state coherence length $\xi_{ab}(0)$ in La₂PrNi₂O₇₋δ films[3] we applied strict resistive criterion:

$$\frac{\rho(T=T_{c,0.01})}{\rho(T=40\ K)} = 0.01 \tag{31}$$

to the $\rho(T,B)$ data reported by Liu *et al*[3] in their Figure 1,c[3]. Obtained $B_{c2}(T)$ dataset and data fit to Eq. 3 are shown in Figure 4,a. Better fit quality was obtained for two-band model[88–90]:

$$B_{c2,total}(T) = B_{c2,band1}(T) + B_{c2,band2}(T) \tag{32}$$

where $band1$ and $band2$ designate upper critical field originated from the respectful band; each band has its independent $\xi_{ab,i}(0)$ and $T_{c,i}$ values, and where $B_{c2,band1}(T)$ and $B_{c2,band2}(T)$ can be described by one of two equations (Eqs. 2,3). The result of $B_{c2}(T)$ data fit to two-band PK-WHH model (Eqs. 3,32) is shown in Figure 4,b.

For the $J_c(sf,T)$ analysis in the La₂PrNi₂O₇₋δ film[3], we rounded in-plane ground state coherence length to $\xi_{ab}(0) = 4.0\ nm$.

Liu *et al*[3] measured *E-J* curves in zero applied field for the La₂PrNi₂O₇₋δ film[3] and reported the $J_c(sf,T)$ dataset obtained by application of the *E*c = 5 µV/cm criterion which is in the same ballpark with commonly used *E*c = 1 µV/cm criterion in applied superconductivity[91–93].

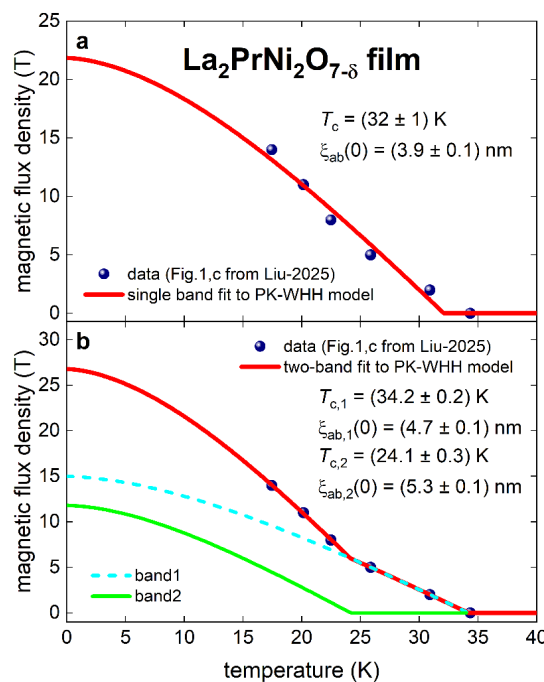**Figure 4.** $B_{c2}(T)$ data deduced from $\rho(T,B)$ curves reported for the ambient pressure La₂PrNi₂O₇₋δ film[3] by applying criterion of $\frac{\rho(T=T_{c,0.01})}{\rho(T=40\ K)} = 0.01$. (**a**) data fit to the single band model (Eq. 3, fit quality $R = 0.9779$); (**b**) data fit to two-band model (Eq. 32, fit quality $R = 0.9999$). Derived parameters are shown.

In Figure 5 we showed the $J_c(sf,T)$ reported by Liu *et al* in their Figure 1,b[3] together with fits to single band models (Eqs. 16-25). One can see that deduced parameters for *s*- and *d*-wave are significantly different from the weak-coupling limits (Eqs. 26,27). Deduced parameters for *p*-wave symmetry fit within their uncertainties are within the weak-coupling limiting values for this symmetry. The confirmation for this gap symmetry is required denser $J_c(sf,T)$ dataset, which span on as wide as it is experimentally possible temperature range, because the $J_c(sf,T)$ temperature dependence at $T < 0.3 \times T_c$ demonstrates unique distinct features of *s*-, *d*-, *p*-wave symmetry. It should be noted that deduced the Ginsburg-Landau parameter remains its large value $\kappa_c \cong 500$, similar to the one in the La₃Ni₂O₇₋δ film[1] (Figures 2,3).
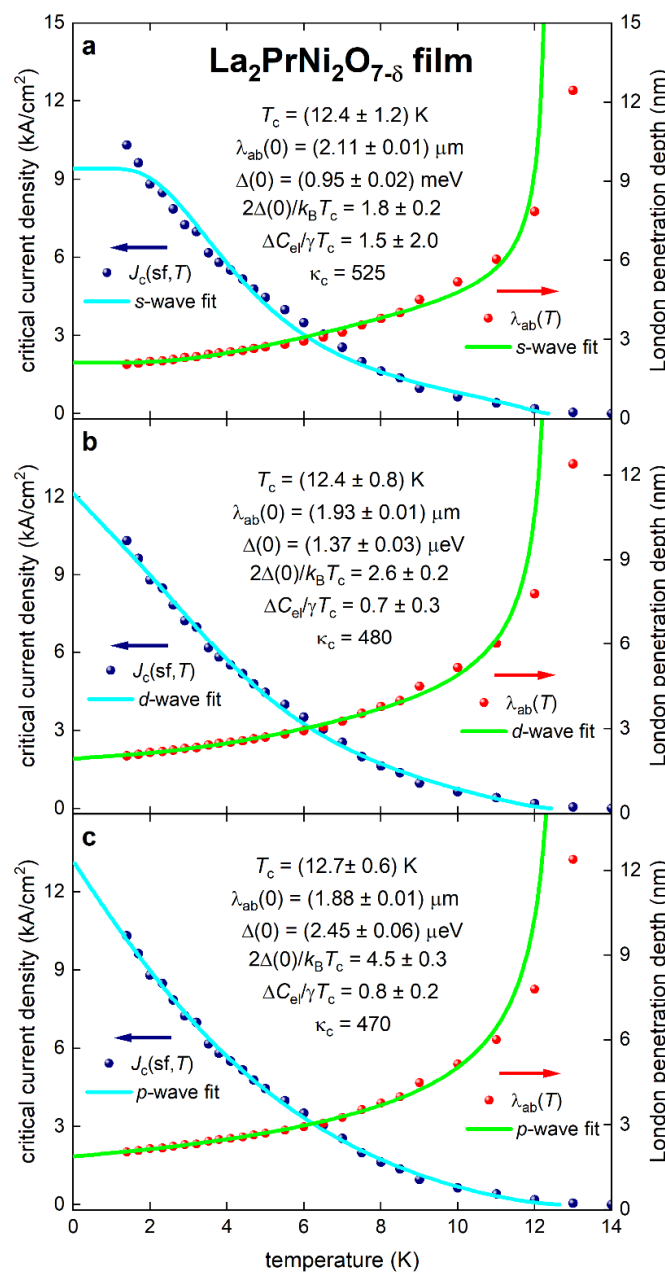
Figure 5. The self-field critical current density, $J_c(sf,T)$, in the ambient pressure La₂PrNi₂O₇₋δ film[3] (reported by Liu *et al*[3] in their Figure 1,b[3]) and data fit to the single band model (Eq. 16) with symmetry of (**a**) *s*-wave (Eqs. 17,18, fit quality $R = 0.9303$); (**b**) *d*-wave (Eqs. 18-20, fit quality $R = 0.9830$); and (**c**) polar $\vec{A} \perp \vec{l}$ *p*-wave (Eqs.

22-25, fit quality $R = 0.9921$). Derived parameters are shown in each panel. $\xi_{ab}(0) = 4\,nm$ was assumed for all fits.

We further analyzed the $J_c(sf,T)$ data within two-band models. In Figure 6 we showed the $J_c(sf,T)$ data fit to two-band *s*-wave model (Eq. 29), where (because two-band fit requires denser $J_c(sf,T)$ dataset that all parameters will be free) we reduced the number of free-fitting parameters by assuming that: (a) both bands have transition temperature equals to the experimental value $T_{c,band1} = T_{c,band2} = 14\,K$; (b) accepting the restriction described by Eq. 30; (c) and fixing the Ginzburg-Landau parameter to $\kappa_c = 500$.

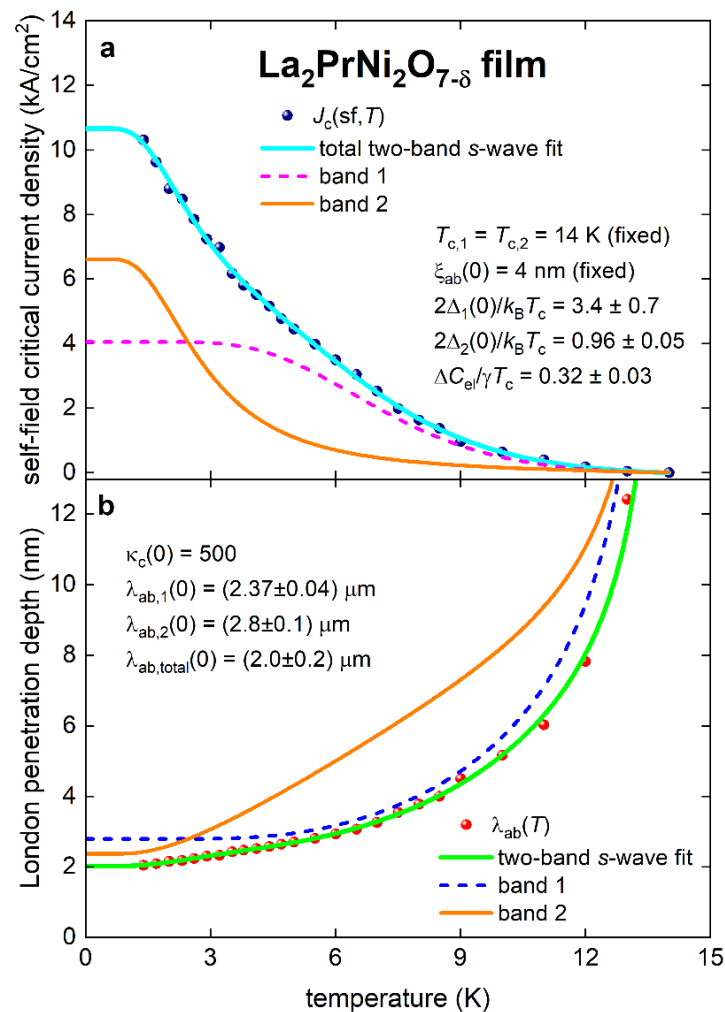**Figure 6.** The self-field critical current density, $J_c(sf,T)$, in the ambient pressure La2PrNi2O7-δ film[3] (reported by Liu *et al*[3] in their Figure 1,b[3]) and data fit to two-band (*s-* + *s-*)-wave model (Eq. 29). The assumptions are: $\left(\frac{\Delta C_{el}}{\gamma T_c}\right)_{band1} = \left(\frac{\Delta C_{el}}{\gamma T_c}\right)_{band2}$, $T_{c,band1} = T_{c,band2} = 14\,K$, and $\xi_{ab}(0) = 4\,nm$. Fit quality is $R = 0.9934$. Derived parameters are shown. (**a**) data and fitting curves are shown for $J_c(sf,T)$ data; (**b**) data and fitting curves are shown for $\lambda_{ab}(T)$ data.

The fit (Figure 6) shows that the gap-to-transition temperature ratios, $\frac{2\Delta_i(0)}{k_BT_c}$, for two bands are, within their uncertainties, in reasonable agreement with the value reported for MgB2 superconductor[86].

In Figure 7 we showed the $J_c(sf,T)$ data fit to (*d*-+*d*-)-wave model (Eq. 29), where we reduced the number of free-fitting parameters assuming that: (a) one band has $T_{c,band1}$ equals to the experimental value $T_{c,band1} = 14\,K$; (b) $\left(\frac{\Delta C_{el}}{\gamma T_c}\right)_{band1} = \left(\frac{\Delta C_{el}}{\gamma T_c}\right)_{band2}$, and (c) $\kappa_c = 500$.
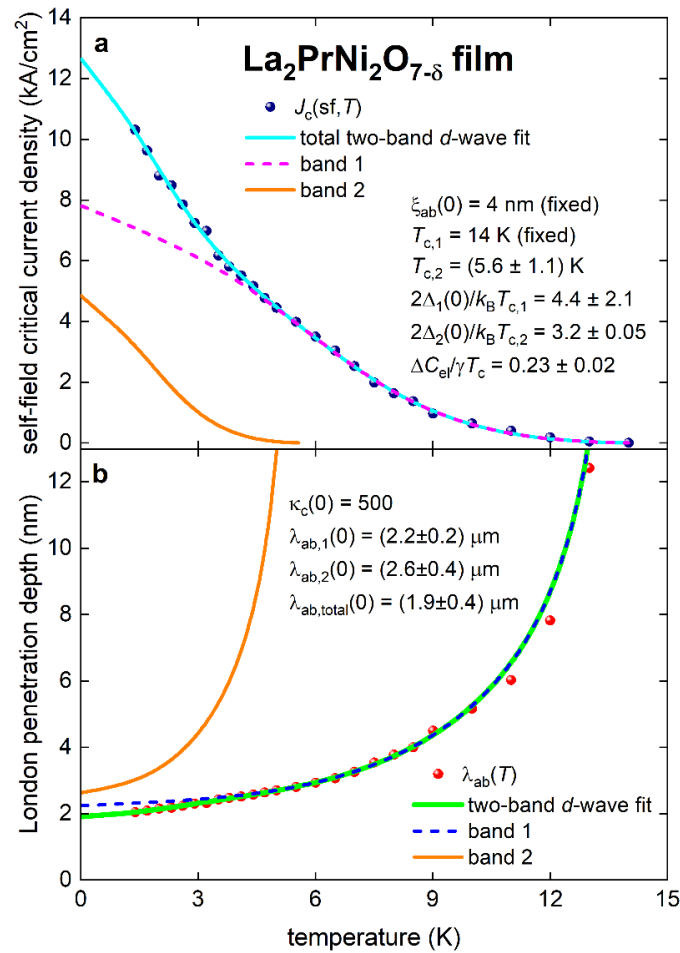
Figure 7. The self-field critical current density, $J_c(sf, T)$, in the ambient pressure La₂PrNi₂O₇₋δ film[3] (reported by Liu *et al*[3] in their Figure 1,b[3]) and data fit to two-band (d- + d-)-wave model (Eq. 29). The assumptions are: $\left(\frac{\Delta C_{el}}{\gamma T_c}\right)_{band1} = \left(\frac{\Delta C_{el}}{\gamma T_c}\right)_{band2}$, $T_{c,band1}$ 14 K, and $\xi_{ab}(0) = 4\ nm$. Fit quality is $R = 0.9930$. Derived parameters are shown. (**a**) data and fitting curves are shown for $J_c(sf, T)$ data; (**b**) data and fitting curves are shown for $\lambda_{ab}(T)$ data.

We showed that there is a variety of gap symmetry models which can with good accuracy describe currently available experimental $J_c(sf, T)$ dataset[3] measured in ambient pressure La₂PrNi₂O₇₋δ film. Thus, denser $J_c(sf, T)$ data which is measured at, as wide as it is experimentally possible, temperature range is required to reveal the gap symmetry in the ambient pressure La₂PrNi₂O₇₋δ films. However, we are confident that ambient pressure La₃₋ₓPrₓNi₂O₇₋δ (x = 0.0; 1.0) films are high-κ type-II superconductors with large London penetration depth $\lambda_{ab}(0) = 1.9 - 6.5\ nm$, and these films are more likely multiple-band superconductors.

IV. Fundamental Parameters in La₃₋ₓPrₓNi₂O₇₋δ (x = 0.15) Films

Zhou *et al*.[2] reported *V-I* curves for 6 nm thick La₃₋ₓPrₓNi₂O₇₋δ (x = 0.15) film[2] which exhibits the $T_{c,onset} \cong 40\ K$. Despite the authors[2] noted "…*that, due to the significant heating effect caused by the applied current (a result of the high critical current associated with the elevated TC), the actual sample temperatures are higher than the recorded values*", there is still an interest to estimate the $J_c(sf, T)$ dataset and $\lambda_{ab}(0)$, because Zhou *et al*.[2] reported $\lambda_{ab}(T = 1.8\ K) = 3.7 \pm^{1.4}_{1.9}\ \mu m$ measured by mutual inductance technique, and, thus, even estimated $\lambda_{ab}(0)$ value deduced from $J_c(sf, T)$ can shed a light on the absolute value of the London penetration depth in ambient pressure La₃₋ₓPrₓNi₂O₇₋δ films.

In Figure 8 we showed the out-of-plane upper critical field data, $B_{c,c}(T)$, deduced from $R(T,B)$ dataset showed in Figure 2,b[2] for which we used resistive criteria of $\frac{R(T=T_{c,0.06})}{R(T=60\,K)} = 0.06$ (in Figure 8,a) and $\frac{R(T=T_{c,0.10})}{R(T=60\,K)} = 0.10$ (in Figure 8,b).

It can be seen that two-band fit to PK-WHH model (Eqs. 3,32) have a good quality, and deduced $\xi_{ab,total}(0) = 4.0\,nm$ is close proximity to the value deduced in La2PrNi2O7-δ film[3] (Figure 4). Also, Figure 8 demonstrate two-band feature of the superconducting state in La3-xPrxNi2O7-δ (x = 0.15) film[2].
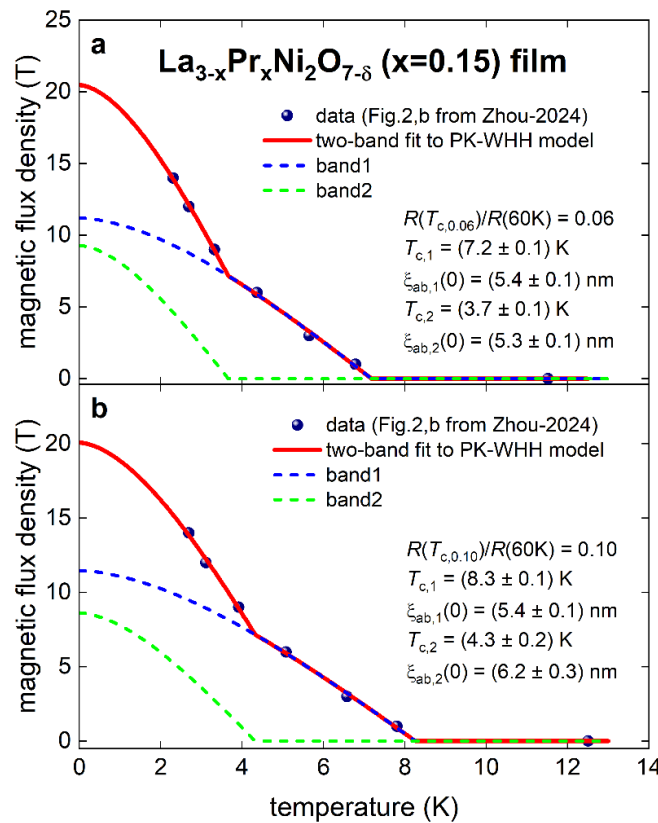
Figure 8. $B_{c2}(T)$ data deduced from $R(T,B)$ curves reported for the ambient pressure La3-xPrxNi2O7-δ (x = 0.15) film[2] by applying criteria of: (**a**) $\frac{R(T=T_{c,0.06})}{R(T=60\,K)} = 0.06$; and (**b**) $\frac{R(T=T_{c,0.10})}{R(T=60\,K)} = 0.10$. Data fits to two band model (Eqs. 3,32). Fits quality (**a**) R = 0.9992; and (**b**) R = 0.9991. Derived parameters are shown.

We estimated $J_c(sf,T)$ dataset in the La3-xPrxNi2O7-δ (x = 0.15) film[2] from *V-I* curves showed in Extended Data Figure 7[2] by assuming transport current bridge lateral dimensions of 5x5 mm and by applying electric field criterion of E_c = 25 μV/cm which is manifold larger than commonly used criterion of E_c = 1 μV/cm, but raw experimental data have noise level at about E = 20 μV/cm (it should be also taking into account a note about sample heating mentioned above).

Derived $J_c(sf,T)$ dataset and fits to single band models are shown in Figure 9, where because of small number of raw data points we reduced as much as it is practically possible the number of free-fitting parameters by fixing $\frac{2\Delta(0)}{k_B T_c}$ and $\frac{\Delta C_{el}}{\gamma T_c}$ values to their weak-coupling limits for respectful gap symmetry (Eqs. 26-28).
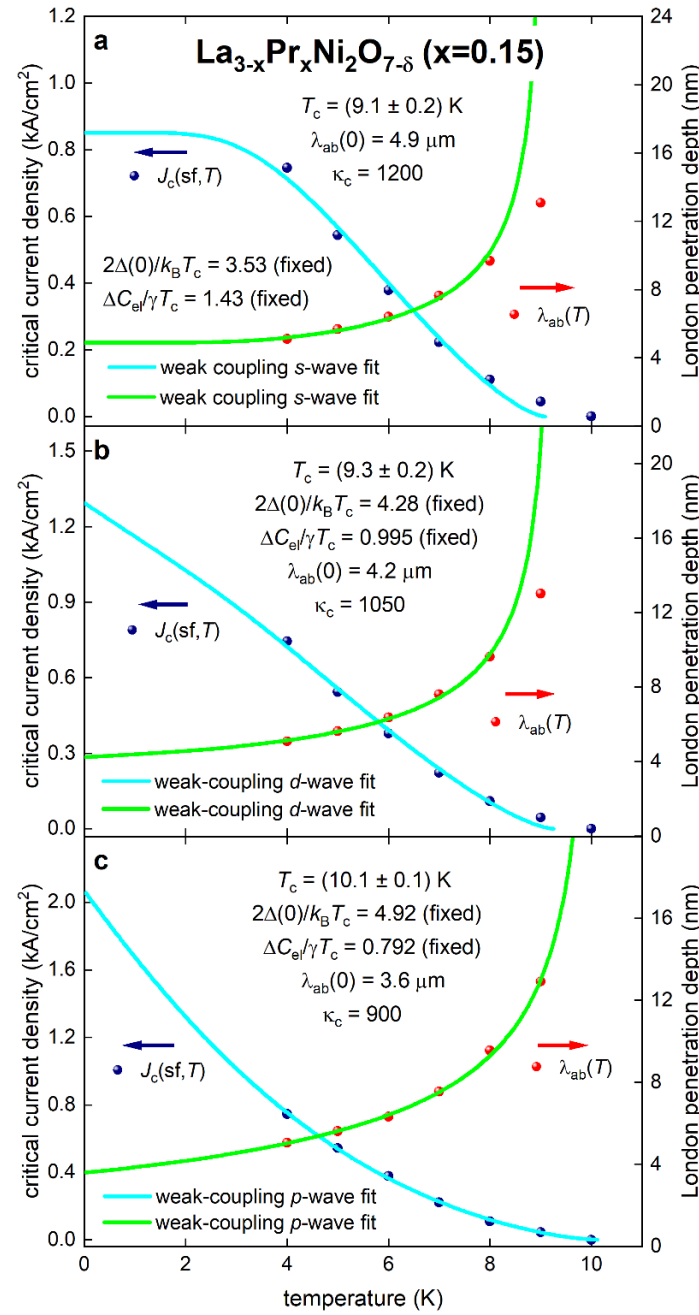
Figure 9. The self-field critical current density, $J_c(sf, T)$, in the ambient pressure La$_{3-x}$Pr$_x$Ni$_2$O$_{7-\delta}$ (x=0.15) film[3] (reported by Zhou *et al*[2] in their Figure 1,b[2,3]) and data fit to the single band weak-coupling model (Eqs. 16,26-28) with symmetry of (**a**) *s*-wave (Eqs. 17,18, fit quality R = 0.7962); (**b**) *d*-wave (Eqs. 18-20, fit quality R = 0.8916); and (**c**) polar $\vec{A} \perp \vec{l}$ *p*-wave (Eqs. 22-25, fit quality R = 0.9809). Derived parameters are shown in each panel. $\xi_{ab}(0) = 4\,nm$ was assumed for all fits.

In the result, deduced $\lambda_{ab}(0) = 3.6 - 4.9\,\mu m$ values are within uncertainty range for the value reported by Zhou *et al*.[2] $\lambda_{ab}(T = 1.8\,K) = 3.7\pm^{1.4}_{1.9}\,\mu m$ measured by mutual inductance technique.

V. More Evidences for Multiple-Band Superconductivity in Ruddlesden–Popper Nickelates

5.1. Highly Compressed Single Crystals La₃Ni₂O₇₋δ

Zhang *et al*[24] reported on zero-resistance state in highly compressed $La_3Ni_2O_{7-\delta}$ single crystals at temperature with highest $T_{c,zero} = 40\ K$. For one of these crystals, raw experimental dataset for $B_{c2}(T)$ defined by the strictest criterion:

$$R(T, B_{appl}) = 0.0 \tag{33}$$

compressed at pressure P = 20.5 GPa and P = 26.6 GPa has been reported in Extended Data Figure 6[24]. In Figure 10 we fitted these two $B_{c2}(T)$ datasets to the two-band model (Eqs. 3, 32), from which two-band superconductivity in highly compressed La₃Ni₂O₇₋δ single crystals can be seen.

We can express a request for experimentalists to measure the $R(T, B)$ data at low applied magnetic field in Ruddlesden–Popper and infinite layer nickelates[1–3,18,22,23,94,95]. Indeed, at the low applied fields, $0\ T \leq B_{appl} \leq 2\ T$, the $\xi_{ab}(0)$ for the band which exhibits higher transition temperature, T_c, can be determined. However, commonly accepted approach is different, and it is related to the applying as high as possible magnetic field, B_{appl}, with practically no any experimental data for an applied field in the range of $0\ T \leq B_{appl} < 2\ T$, except at $B_{appl} = 1\ T$.

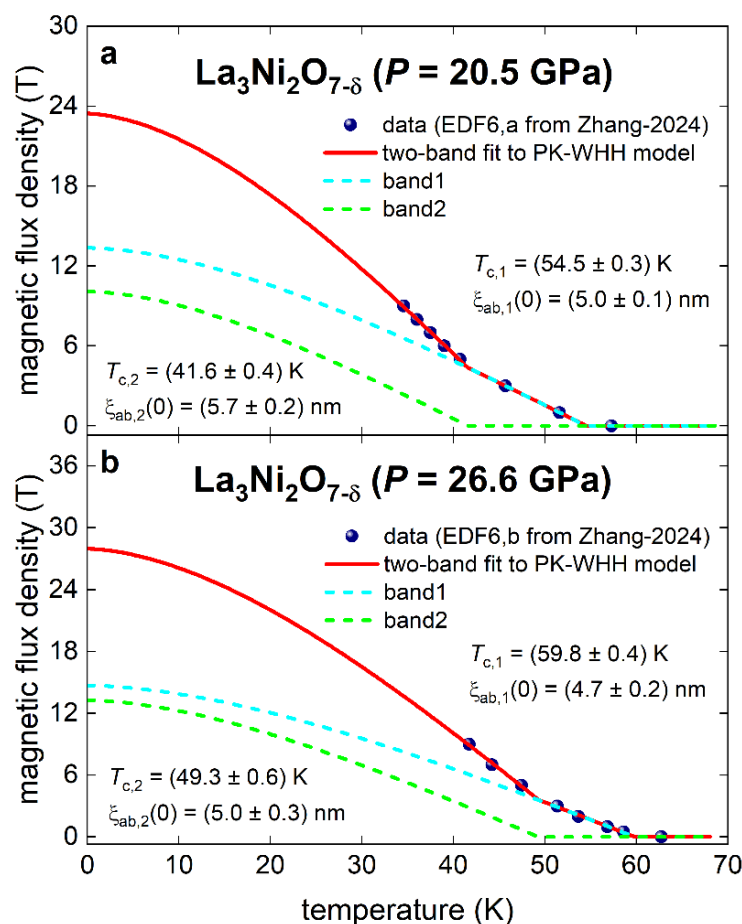**Figure 10.** $B_{c2}(T)$ defined at $R(T, B_{appl}) = 0.0$ for highly compressed La₃Ni₂O₇₋δ single crystal[24] (reported by Zhang *et al.*[24]) and data fit to two-band model (Eqs. 3,32) for applied pressure (**a**) $P = 20.5\ GPa$ (fit quality R = 0.9998); and (**b**) $P = 26.6\ GPa$ (fit quality R = 0.9989). Derived parameters are shown.

5.1. Highly Compressed Polycrystalline La₂PrNi₂O₇₋δ

Wang *et al*[96] reported on zero-resistance state in highly compressed La₃PrNi₂O₇₋δ polycrystalline samples with highest $T_{c,zero} = 60\,K$. We digitized the $R(T, B_{appl})$ data from Extended Data Figure 6,a[96] and applied the criterion of:

$$\frac{R(T_{c,0.20})}{R(T=80\,K)} = 0.20. \tag{34}$$

Determined $B_{c2}(T, P = 15\,GPa)$ dataset and the fit to the two-band model are shown in Figure 11.

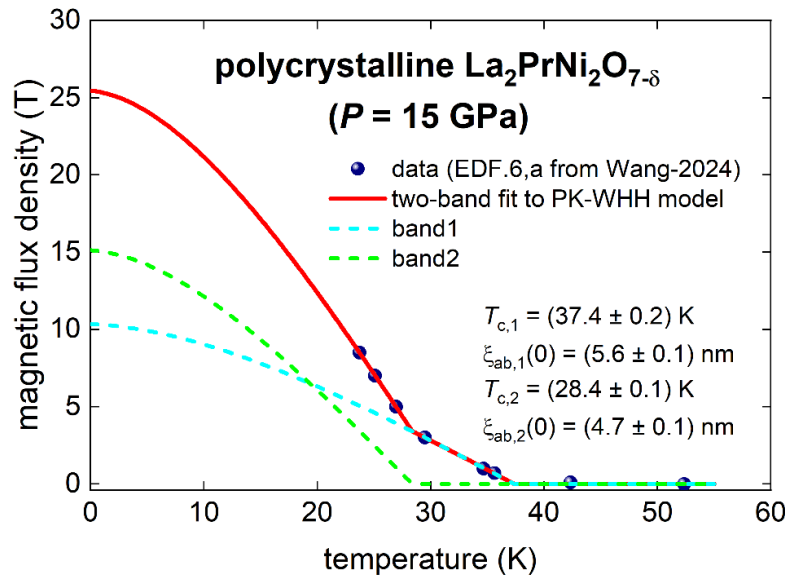**Figure 11.** $B_{c2}(T)$ defined by $\frac{R(T_{c,0.20})}{R(T=80\,K)} = 0.20$ criterion for highly compressed La₂PrNi₂O₇₋δ polycrystal [96] (reported by Wang *et al*.[96]) and data fit to two-band model (Eqs. 3,32) for applied pressure $P = 15\,GPa$ (fit quality $R = 0.9998$). Derived parameters are shown.

5.3. Highly Compressed Single Crystals La₄Ni₃O₁₀₋δ

Zhu *et al*[97] reported on zero-resistance state in highly compressed La₄Ni₃O₁₀₋δ single crystals with the highest $T_{c,zero} \cong 12\,K$. Raw experimental $R(T, B_{appl})$ data is available for this study[97]. We applied the lowest possible criterion for each $R(T, B_{appl}, P)$ dataset in the range of:

$$0.01 \le \frac{R(T_c)}{R(T=50\,K)} \le 0.07 \tag{35}$$

to determine the $B_{c2}(T, P)$. Data fit to two-band model for La₄Ni₃O₁₀₋δ single crystal compressed at four pressures are shown in Figure 12, from which two-band superconductivity in highly compressed La₄Ni₃O₁₀₋δ is evident.
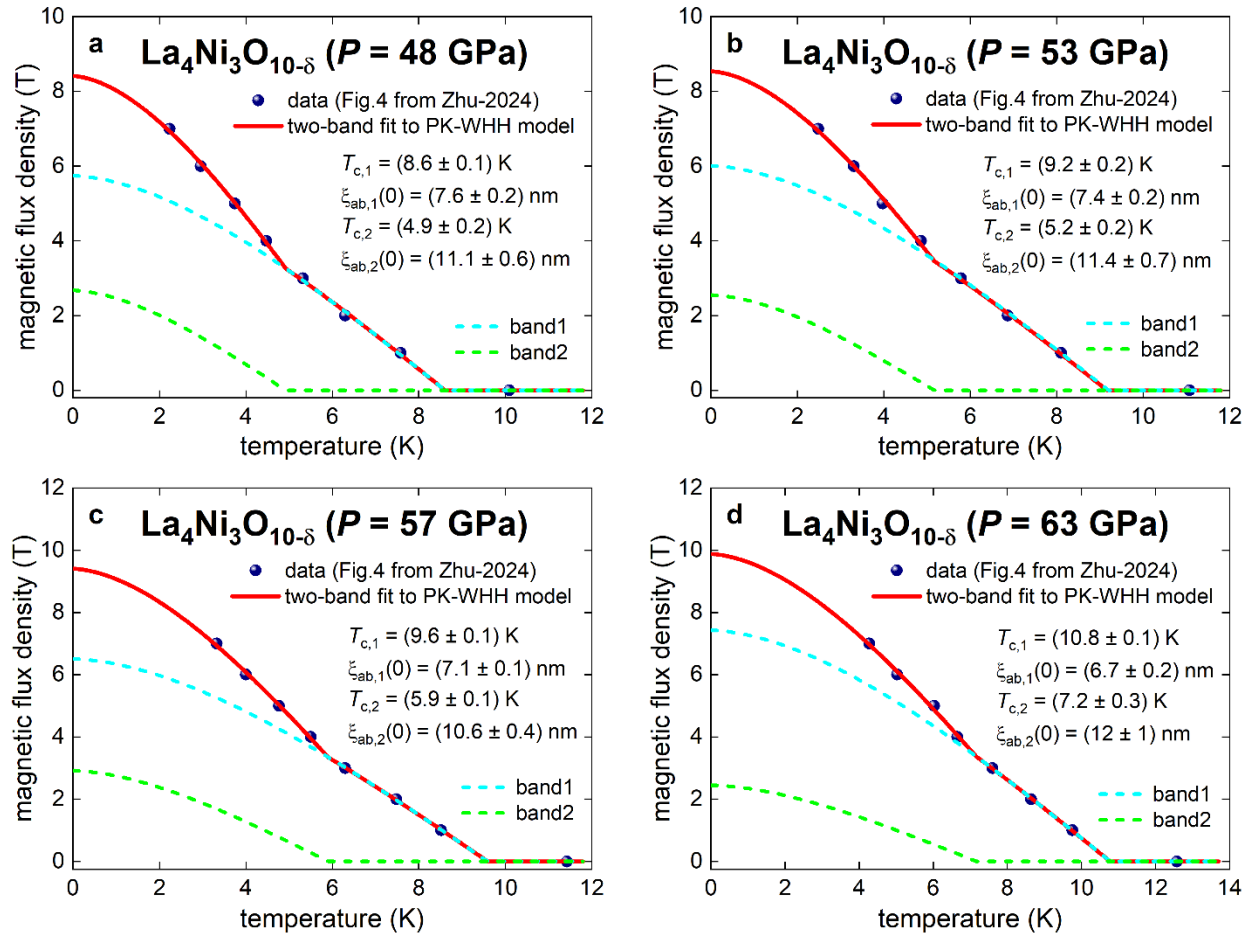
Figure 12. $B_{c2}(T)$ defined by the following criteria: (a) $\frac{R(T_{c,0.07})}{R(T=50\,K)} = 0.07$, (b) $\frac{R(T_{c,0.02})}{R(T=50\,K)} = 0.02$, (c,d) $\frac{R(T_{c,0.01})}{R(T=50\,K)} = 0.01$ in highly compressed La$_4$Ni$_3$O$_{10-\delta}$ single crystal[97] (reported by Zhu *et al.*[97]) and data fit to two-band model (Eqs. 3,32) for measurements performed at applied pressure: (a) $P = 48\,GPa$ (fit quality $R = 0.9993$); (b) $P = 53\,GPa$ (fit quality $R = 0.9991$); (c) $P = 57\,GPa$ (fit quality $R = 0.9997$); (d) $P = 63\,GPa$ (fit quality $R = 0.9992$). Derived parameters are shown.

5.4. Ambient Pressure La$_3$Ni$_2$O$_{7-\delta}$ Thin Film

For the completeness, in Figure 13 we showed the $B_{c2}(T)$ dataset for La$_3$Ni$_2$O$_{7-\delta}$ thin film[1] defined by non-strict criterion, which allows to cover the high-field range of the $R(T,B)$ data, reported by Ko *et al*[1] in their Figure 3,b[1]:

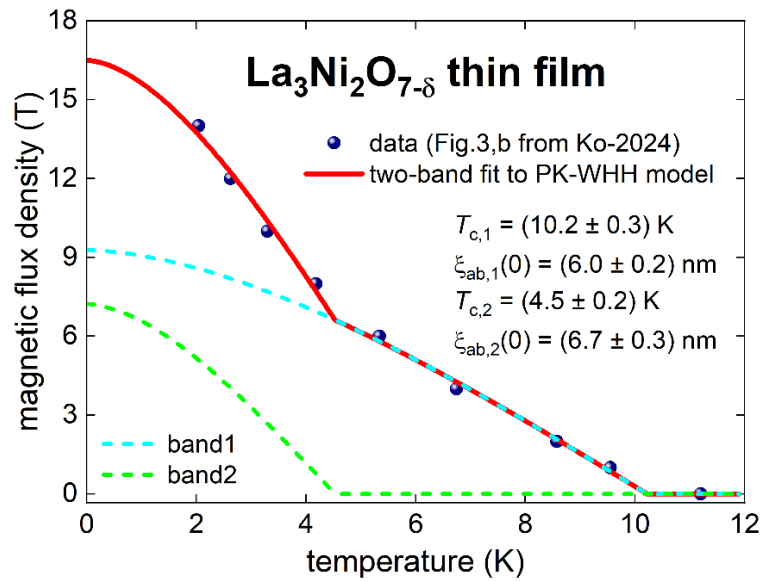$$\frac{R(T=T_c)}{\rho(T_{c,onset}=40\,K)} = 0.29. \tag{36}$$

Figure 13. $B_{c2}(T)$ data deduced from $R(T, B)$ curves reported for the ambient pressure La$_3$Ni$_2$O$_{7-\delta}$ film reported in Figure 3,b[1] by applying criteria of $\frac{R(T=T_{c,0.29})}{R(T=60\,K)} = 0.29$. Data fits to two-band model (Eqs. 3,32). Fit quality is $R = 0.9973$. Derived parameters are shown.

5.5. Ambient Pressure La$_6$Ni$_5$O$_{12}$ Thin Film

Recently, Yan *et al.*[98] reported on observation of significant drop in resistivity in ambient pressure single-unit-cell Nd$_6$Ni$_5$O$_{12}$ film at temperatures $T \lesssim 10\,K$. Despite the zero resistance was not observed in the film (down to $T = 1.8\,K$), typical for superconductors suppression of the T_c^{onset} in applied magnetic field was observed. We assumed that the single-unit-cell Nd$_6$Ni$_5$O$_{12}$ film is a superconductor and applied resistive criterion:

$$\frac{R(T=T_{c,0.50})}{\rho(T_{c,onset}=30\,K)} = 0.50 \tag{37}$$

to determine the $B_{c2}(T)$ dataset for Nd$_6$Ni$_5$O$_{12}$ film. In Figure 14 we showed the obtained $B_{c2}(T)$ dataset and data fit to two-band model (Eqs. 3, 32). Evidence for two-band superconductivity can be seen in Figure 14. We should note that the emergence of the second band is completely missed if the $B_{c2}(T)$ will be defined by overwhelmingly large criterion of $\frac{R(T=T_{c,0.90})}{\rho(T_{c,onset}=30\,K)} = 0.90$, as the one implemented by Yan *et al.*[98] in their Figure 1,d.
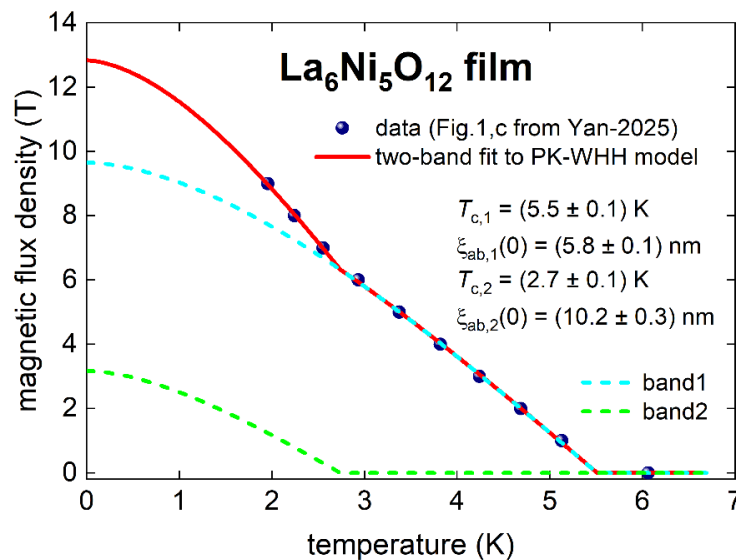
Figure 14. $B_{c2}(T)$ data deduced from $R(T,B)$ curves reported for the ambient pressure single-unit-cell La$_6$Ni$_5$O$_{12}$ film reported in Figure 1,c[98] and by applying criteria of $\frac{R(T=T_{c,0.50})}{R(T=30\,K)} = 0.50$. Data fits to two-band model (Eqs. 3,32). Fit quality is $R = 0.9973$. Derived parameters are shown.

5.6. Highly Compressed Pr$_4$Ni$_3$O$_{10}$ Single Crystal

To demonstrate that the Ruddlesden-Popper nickelates exhibit two-band superconductivity in Figure 15 we showed the $B_{c2}(T)$ datasets deduced from the $R(T,B)$ dataset measured in highly compressed Nd$_6$Ni$_5$O$_{12}$ single crystal by Chen *et al.*[99]. It should be noted, that recently Zhang *et al.*[100] reported on observation of the zero-resistance state with $T_{c,zero}(P = 70.5\,GPa) = 18\,K$ in the single crystal of the same phase Nd$_6$Ni$_5$O$_{12}$, however, the $R(T,B)$ dataset is unavailable to date.

In Figure 15,a we applied the criterion of $\frac{R(T=T_{C,0.56})}{\rho(T_{c,onset}=30\,K)} = 0.56$ to define the $B_{c2}(T, P = 32.4\,GPa)$ dataset reported in Figure 2,a[99], and in Figure 15,b we applied the criterion of $\frac{R(T=T_{C,0.50})}{\rho(T_{c,onset}=30\,K)} = 0.84$ to define $B_{c2}(T, P = 55\,GPa)$ in the Nd$_6$Ni$_5$O$_{12}$ single crystal.

Data fits to Eqs. 3,32 (Figure 15) confirms two-band nature of the superconducting state in highly compressed Nd$_6$Ni$_5$O$_{12}$ single crystal.
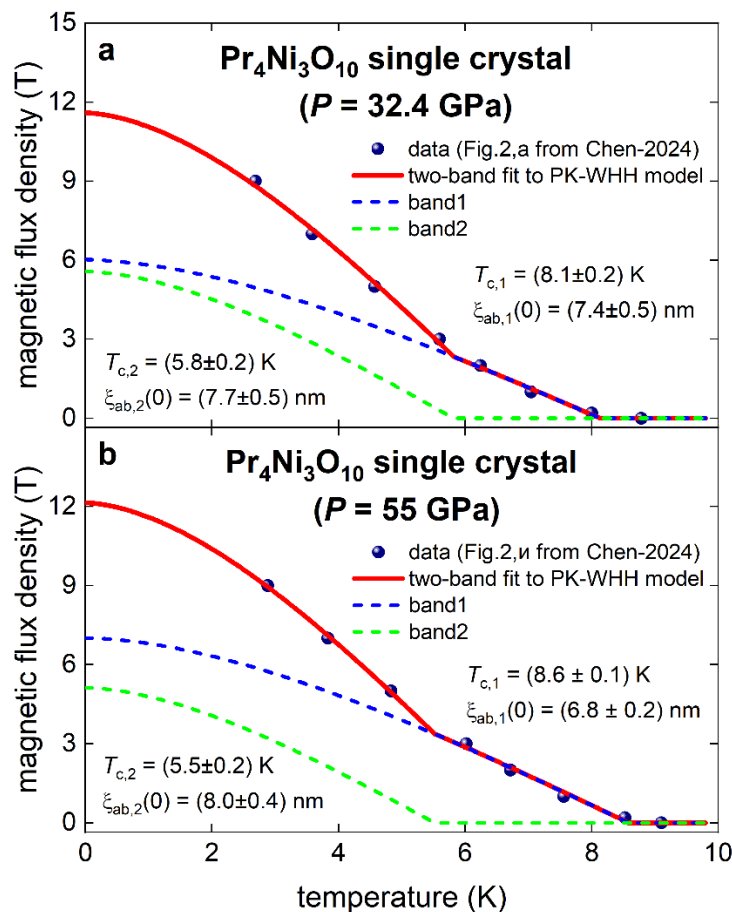
Figure 15. $B_{c2}(T)$ defined by the following criteria: (**a**) $\frac{R(T_{C,0.56})}{R(T=30\,K)} = 0.56$ and (**b**) $\frac{R(T_{C,0.84})}{R(T=30\,K)} = 0.84$ in highly compressed Pr$_4$Ni$_3$O$_{10-\delta}$ single crystal[99] (reported by Chen *et al.*[99]) and data fit to two-band model (Eqs. 3,32) for measurements performed at applied pressure: (**a**) $P = 32.4\,GPa$ (fit quality is $R = 0.9983$) and (**b**) $P = 55\,GPa$ (fit quality is $R = 0.9988$). Derived parameters are shown.

VI. The Limitation of T_c in Nickelates by Thermal Fluctuations

Thermal fluctuations are expected to break Cooper pairs and suppress superconductivity for materials with low superfluid density[32]. For HTS cuprates strong thermal fluctuations reduce the

observed transition temperature, T_c, below its meanfield value, by up to 30%, and similar feature have been understood in iron-based superconductors[101–104], however, the transition temperatures in near-room-temperature hydride superconductors[105–111] based on their 3D nature and short London penetration depth $\lambda(0)$[112–114] are not affected by thermal fluctuations[33,115].

However, large London penetration depth $\lambda(T)$ in ambient pressure $La_{3-x}Pr_xNi_2O_{7-\delta}$ (x = 0.0, 0.15, 1.0) films deduced herein and reported in Ref.[2] opened a question about the impact of thermal fluctuations on T_c in these films.

By considering unit cells of the Ruddlesden-Popper nickelate family phases, $La_{n+1}Ni_nO_{3n+1}$ (n = 2,3) considering herein, one can conclude that main structural element where high-temperature superconductivity is originated from is the 3D Ni-O octahedron. Thus, in opposite to HTS cuprates, the superconductivity in $La_{n+1}Ni_nO_{3n+1}$ can be classified to exhibit 3D nature, despite the superconductivity observed in very thin films of $La_{n+1}Ni_nO_{3n+1}$.

Based on this, we can calculate the phase fluctuation temperature for 3D superconductors in accordance with Emery and Kivelson approach[32]:

$$T_{fluc,phase}[K] = \frac{2.2 \times \phi_0^2 \sqrt{\pi} \xi(0)}{4\pi^2 \mu_0 k_B \lambda^2(0)} = \frac{0.55 \times \phi_0^2}{\pi^{1.5} \mu_0 k_B} \times \frac{1}{\lambda_{ab}(0) \times \kappa_c(0)} = \frac{0.0243\,[m\,K]}{\lambda_{ab}(0) \times \kappa_c(0)\,[m]} \tag{38}$$

The substitution of the deduced values for the $La_3Ni_2O_{7-\delta}$ film[1] in Eq. 38 returns:

$$T_{fluc,phase}(\lambda_{ab}(0) = 6.4\,\mu m; \kappa_c(0) = 500) = 7.6\,K \tag{39}$$

Defined by us (Eq. 13) $T_{c,0.06} = 3.0 - 3.5\,K$ in this film is about half of the $T_{fluc,phase} = 7.6\,K$, which is expected value, if we take into account that thermal fluctuations cause ~ 30-50% suppression for T_c.

The substitution of the deduced values for the $La_2PrNi_2O_{7-\delta}$ film[3] in Eq. 38 returns:

$$T_{fluc,phase}(\lambda_{ab}(0) = 2.0\,\mu m; \kappa_c(0) = 500) = 24\,K, \tag{40}$$

which is again about twice higher than the observed $T_{c,zero} = 14\,K$.

For the for the $La_{3-x}Pr_xNi_2O_{7-\delta}$ film[2], the substitution of the lower limit for the reported $\lambda_{ab}(T = 1.8\,K) = 3.7\pm_{1.9}^{1.4}\,\mu m$ value and $\kappa_c(0) = 500$, returns:

$$T_{fluc,phase}(\lambda_{ab}(0) = 1.8\,\mu m; \kappa_c(0) = 500) = 27\,K \tag{41}$$

We need to mention, that the authors[2] pointed out that reported $J_c(sf, T)$ (from which we extracted $\lambda_{ab}(0) = 4.0\,\mu m$) was measured at conditions of large heat realize. Thus, the shortest London penetration depth $\lambda_{ab}(0) = 3.6\,\mu m$ (Figure 9) which we deduced from the $J_c(sf, T)$ represents the upper-limiting value for the London penetration depth, for which we calculate:

$$T_{fluc,phase}(\lambda_{ab}(0) = 3.6\,\mu m; \kappa_c(0) = 900) = 7.5\,K \tag{42}$$

Thus, the $La_{3-x}Pr_xNi_2O_{7-\delta}$ film[2] exhibits the phase fluctuation temperature in the range:

$$7.5\,K \leq T_{fluc,phase} \leq 27\,K. \tag{43}$$

And thus, observed in experiment diamagnetic $T_{c,diamag} = 8.5\,K$ and resistive $T_{c,zero} =\cong 9.0\,K$ are in the range described by Eq. 43.

In Figure 16, we summarized the London penetration depth data $\lambda_{ab}(T)$ for $La_{3-x}Pr_xNi_2O_{7-\delta}$ (x = 0.0, 0.15, 1.0) films.

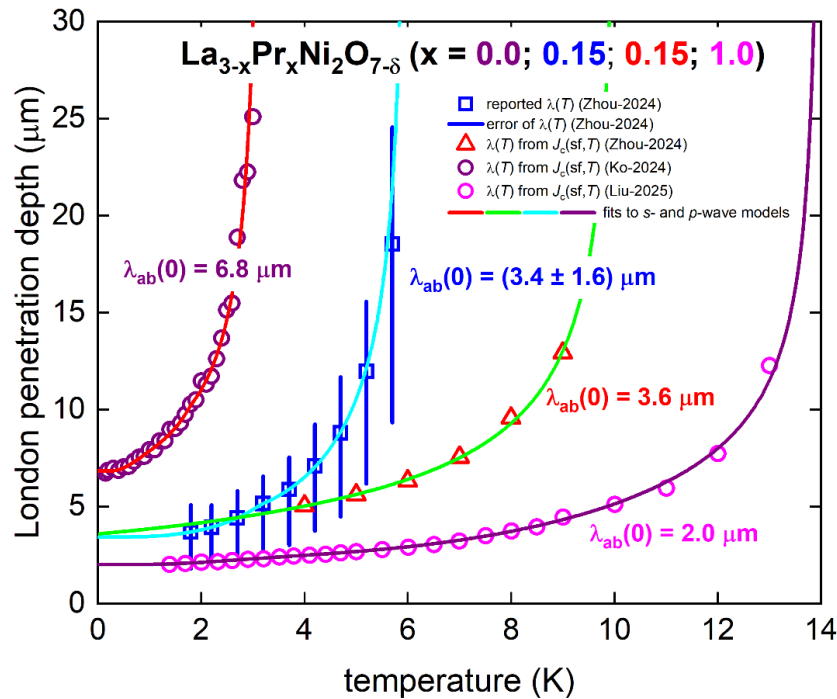**Figure 16.** Derived London penetration depth, $\lambda_{ab}(T)$, for all ambient pressure La$_{3-x}$Pr$_x$Ni$_2$O$_{7-\delta}$ (x=0.0; 0.15; 1.0) thin films[1–3] studied in this work.

Substituting deduced $\lambda_{ab}(0)$ and $\xi_{ab}(0)$ parameters in Eq. 9, one can calculate the value for ground state lower critical field:

$$B_{c1}(0) = (20 - 240) \, \mu T \tag{44}$$

Similar low $B_{c1}(0)$ value in highly compressed La$_3$Ni$_2$O$_{7-\delta}$ was first estimated in Ref. 87.

References

1. Ko, E. K. *et al.* Signatures of ambient pressure superconductivity in thin film La$_3$Ni$_2$O$_7$. *Nature* (2024) doi:10.1038/s41586-024-08525-3.

2. Zhou, G. *et al.* Ambient-pressure superconductivity onset above 40 K in bilayer nickelate ultrathin films. (2024).

3. Liu, Y. *et al.* Superconductivity and normal-state transport in compressively strained La$_2$PrNi$_2$O$_7$ thin films. (2025).

4. Anisimov, V. I., Bukhvalov, D. & Rice, T. M. Electronic structure of possible nickelate analogs to the cuprates. *Phys Rev B* **59**, 7901–7906 (1999).

5. Li, D. *et al.* Superconductivity in an infinite-layer nickelate. *Nature* **572**, 624–627 (2019).

6. Sun, H. *et al.* Signatures of superconductivity near 80 K in a nickelate under high pressure. *Nature* **621**, 493–498 (2023).

7. Brisi, C., Vallino, M. & Abbattista, F. Composition and structure of two hitherto unidentified phases in the system La2O3-NiO-O. *Journal of the Less Common Metals* **79**, 215–219 (1981).

8. Ram, R. A. M., Ganapathi, L., Ganguly, P. & Rao, C. N. R. Evolution of three-dimensional character across the Lan+1NinO3n+1 homologous series with increase in n. *J Solid State Chem* **63**, 139–147 (1986).

9.   Sreedhar, K. *et al.* Low-Temperature Electronic Properties of the Lan+1NinO3n+1 (n = 2, 3, and ∞) System: Evidence for a Crossover from Fluctuating-Valence to Fermi-Liquid-like Behavior. *J Solid State Chem* **110**, 208–215 (1994).

10.   Zhang, Z., Greenblatt, M. & Goodenough, J. B. Synthesis, Structure, and Properties of the Layered Perovskite La3Ni2O7-δ. *J Solid State Chem* **108**, 402–409 (1994).

11.   Taniguchi, S. *et al.* Transport, Magnetic and Thermal Properties of La$_3$Ni$_2$O$_{7-δ}$. *J Physical Soc Japan* **64**, 1644–1650 (1995).

12.   Wu, G., Neumeier, J. J. & Hundley, M. F. Magnetic susceptibility, heat capacity, and pressure dependence of the electrical resistivity of La3N2O7 and La4Ni3O10. *Phys Rev B* **63**, 245120 (2001).

13.   Burriel, M. *et al.* Enhanced High-Temperature Electronic Transport Properties in Nanostructured Epitaxial Thin Films of the La$_{n+1}$Ni$_n$O$_{3n+1}$ Ruddlesden−Popper Series (*n* = 1, 2, 3, ∞). *Chemistry of Materials* **19**, 4056–4062 (2007).

14.   Helfand, E. & Werthamer, N. R. Temperature and Purity Dependence of the Superconducting Critical Field, Hc2. II. *Physical Review* **147**, 288–294 (1966).

15.   Werthamer, N. R., Helfand, E. & Hohenberg, P. C. Temperature and Purity Dependence of the Superconducting Critical Field, Hc2. III. Electron Spin and Spin-Orbit Effects. *Physical Review* **147**, 295–302 (1966).

16.   Baumgartner, T. *et al.* Effects of neutron irradiation on pinning force scaling in state-of-the-art Nb3Sn wires. *Supercond Sci Technol* **27**, 015005 (2014).

17.   Prozorov, R. & Kogan, V. G. Practically universal representation of the Helfand-Werthamer upper critical field for any transport scattering rate. *Phys Rev Appl* **22**, 064006 (2024).

18.   Yan, X. *et al.* Superconductivity in an ultrathin multilayer nickelate. *Sci Adv* **11**, (2025).

19.   Wang, Z.-C. *et al.* Superconductivity in KCa$_2$Fe$_4$As$_4$F$_2$ with Separate Double Fe$_2$As$_2$ Layers. *J Am Chem Soc* **138**, 7856–7859 (2016).

20.   Honda, F. *et al.* Pressure-induced Structural Phase Transition and New Superconducting Phase in UTe$_2$. *J Physical Soc Japan* **92**, (2023).

21.   Wang, B. Y. *et al.* Effects of rare-earth magnetism on the superconducting upper critical field in infinite-layer nickelates. *Sci Adv* **9**, (2023).

22.   Wang, B. Y. *et al.* Isotropic Pauli-limited superconductivity in the infinite-layer nickelate Nd$_{0.775}$Sr$_{0.225}$NiO$_2$. *Nat Phys* **17**, 473–477 (2021).

23.   Ji, H. *et al.* Rotational symmetry breaking in superconducting nickelate Nd0.8Sr0.2NiO2 films. *Nat Commun* **14**, 7155 (2023).

24.   Zhang, Y. *et al.* High-temperature superconductivity with zero resistance and strange-metal behaviour in La$_3$Ni$_2$O$_{7-δ}$. *Nat Phys* (2024) doi:10.1038/s41567-024-02515-y.

25.   Cao, Y. *et al.* Unconventional superconductivity in magic-angle graphene superlattices. *Nature* **556**, 43–50 (2018).

26.   Park, J. M. *et al.* Robust superconductivity in magic-angle multilayer graphene family. *Nat Mater* **21**, 877–883 (2022).

27.   Di Battista, G. *et al.* Infrared single-photon detection with superconducting magic-angle twisted bilayer graphene. *Sci Adv* **10**, (2024).

28.   Lee, K. *et al.* Linear-in-temperature resistivity for optimally superconducting (Nd,Sr)NiO2. *Nature* **619**, 288–292 (2023).

29.   Osada, M. *et al.* A Superconducting Praseodymium Nickelate with Infinite Layer Structure. *Nano Lett* **20**, 5735–5740 (2020).

30.   Pan, G. A. *et al.* Superconductivity in a quintuple-layer square-planar nickelate. *Nat Mater* **21**, 160–164 (2022).

31.   Bulaevskii, L. N., Ginzburg, V. L. & Sobyanin, A. A. Macroscopic theory of superconductors with small coherence length. *Physica C Supercond* **152**, 378–388 (1988).

32.   Emery, V. J. & Kivelson, S. A. Importance of phase fluctuations in superconductors with small superfluid density. *Nature* **374**, 434–437 (1995).

33. Talantsev, E. F., Crump, W. P., Storey, J. G. & Tallon, J. L. London penetration depth and thermal fluctuations in the sulphur hydride 203 K superconductor. *Ann Phys* **529**, 1–5 (2017).

34. Andersson, M. Comment on "Superconducting state of Ca-VII below a critical temperature of 29 K at a pressure of 216 GPa". *Phys Rev B* **84**, 216501 (2011).

35. Wu L, Si J, Guan S, Zhang H, Dou J, Kuo J, Yang J, Yu H, Zhang J, Ma X, Yang P, Zhou R, Liu M, Hong F, Yu X 2024 Record-high T_c and dome-shaped superconductivity in a medium-entropy alloy TaNbHfZr under pressure up to 160 GPa. *Phys Rev Lett* **132** 166002.

36. Ye, G. *et al.* Distinct pressure evolution of superconductivity and charge density wave in kagome superconductor CsV_3Sb_5 thin flakes. *Phys Rev B* **109**, 054501 (2024).

37. Nie, J. Y. *et al.* On the superconducting gap structure of the miassite $Rh_{17}S_{15}$: Nodal or nodeless? (2024).

38. Chen, K. Y. *et al.* Double Superconducting Dome and Triple Enhancement of T_c in the Kagome Superconductor CsV_3Sb_5 under High Pressure. *Phys Rev Lett* **126**, 247001 (2021).

39. Huyan, S. *et al.* Suppression of metal-to-insulator transition and stabilization of superconductivity by pressure in Re_3Ge_7. *Phys Rev B* **109**, 174522 (2024).

40. Terashima, T. *et al.* 2024 Anomalous upper critical field in the quasicrystal superconductor $Ta_{1.6}Te$ *npj Quantum Materials* **9** 56.

41. Ruan, B.-B. *et al.* Superconductivity in $Mo_4Ga_{20}As$ with endohedral gallium clusters. *Journal of Physics: Condensed Matter* **35**, 214002 (2023).

42. Zhang, C. L. *et al.* Superconductivity above 80 K in polyhydrides of hafnium. *Materials Today Physics* **27**, 100826 (2022).

43. Wang, L. S. *et al.* Nodeless superconducting gap in the topological superconductor candidate $2M-WS_2$. *Phys Rev B* **102**, 024523 (2020).

44. Pan, J. *et al.* Nodal superconductivity and superconducting dome in the layered superconductor $Ta_4Pd_3Te_{16}$. *Phys Rev B* **92**, 180505 (2015).

45. Vedeneev, S. I., Piot, B. A., Maude, D. K. & Sadakov, A. V. Temperature dependence of the upper critical field of FeSe single crystals. *Phys Rev B* **87**, 134512 (2013).

46. Yu, F. H. *et al.* Unusual competition of superconductivity and charge-density-wave state in a compressed topological kagome metal. *Nat Commun* **12**, 3645 (2021).

47. Dong, Q. *et al.* Strong superconducting pairing strength and pseudogap features in a putative multiphase heavy-fermion superconductor CeRh2As2 by soft point-contact spectroscopy. (2025).

48. Bärtl, F. *et al.* Evidence of pseudogap and absence of spin magnetism in the time-reversal-symmetry-breaking state of $Ba_{1-x}K_xFe_2As_2$. (2025).

49. Jangid, S. *et al.* Superconductivity with a high upper critical field in an equiatomic high-entropy alloy Sc–V–Ti–Hf–Nb. *Appl Phys Lett* **124**, (2024).

50. Jangid, S. *et al.* High critical field superconductivity in a 3d dominated lightweight equiatomic high entropy alloy. (2025).

51. Sharma, S. *et al.* Evidence for conventional superconductivity in Bi_2PdPt and prediction of possible topological superconductivity in disorder-free γ−BiPd. *Phys Rev B* **109**, 224509 (2024).

52. Landaeta, J. F. *et al.* Evidence for vertical line nodes in Sr_2RuO_4 from nonlocal electrodynamics. *Phys Rev B* **110**, L100503 (2024).

53. Sun, Y. *et al.* Specific Heat and Upper Critical Field of $Sc_5Ir_4Si_{10}$ Superconductor. *J Physical Soc Japan* **82**, 074713 (2013).

54. Perkins, G. K. *et al.* Superconducting critical fields and anisotropy of a MgB2 single crystal. *Supercond Sci Technol* **15**, 330 (2002).

55. Arima, H. *et al.* Direct Observation of Vortices and Antivortices Generation in Phase-Separated Superconductor Sn-Pb Solder. (2025).

56. Landaeta, J. F. *et al.* Conventional type-II superconductivity in locally noncentrosymmetric $LaRh_2As_2$ single crystals. *Phys Rev B* **106**, 014506 (2022).

57. Watanabe, Y., Miura, A., Moriyoshi, C., Yamashita, A. & Mizuguchi, Y. Observation of superconductivity and enhanced upper critical field of η-carbide-type oxide Zr_4Pd_2O. *Sci Rep* **13**, 22458 (2023).

58. Ma, K. *et al.* Superconductivity with High Upper Critical Field in the Cubic Centrosymmetric η-Carbide $Nb_4Rh_2C_{1-\delta}$. *ACS Materials Au* **1**, 55–61 (2021).

59. Michor, H. *et al.* Superconductivity in layered YB_2C_2. *J Phys Conf Ser* **150**, 052160 (2009).

60. Anand, V. K. *et al.* Physical properties of noncentrosymmetric superconductor $LaIrSi_3$: A μSR study. *Phys Rev B* **90**, 014513 (2014).

61. Chajewski, G., Szymański, D., Daszkiewicz, M. & Kaczorowski, D. Horizontal flux growth as an efficient preparation method of $CeRh_2As_2$ single crystals. *Mater Horiz* **11**, 855–861 (2024).

62. Li, L. *et al.* Large upper critical fields and strong coupling superconductivity in the medium-entropy alloy $(Ti_{1/3}Hf_{1/3}Ta_{1/3})_{1-x}Nb_x$. (2025).

63. Du, F. *et al.* Tunneling Spectroscopy at Megabar Pressures: Determination of the Superconducting Gap in Sulfur. *Phys Rev Lett* **133**, 036002 (2024).

64. Takahashi, H. *et al.* Superconductivity in a ferroelectric-like topological semimetal SrAuBi. *NPJ Quantum Mater* **8**, 77 (2023).

65. Sundar, S., Chattopadhyay, M. K., Chandra, L. S. S., Rawat, R. & Roy, S. B. Vortex–glass transformation within the surface superconducting state of β-phase $Mo_{(1-x)}Re_x$ alloys. *Supercond Sci Technol* **30**, 025003 (2017).

66. Liu, Y. *et al.* Superconductivity under pressure in a chromium-based kagome metal. *Nature* **632**, 1032–1037 (2024).

67. Zeng, S. W. *et al.* Observation of perfect diamagnetism and interfacial effect on the electronic structures in infinite layer $Nd_{0.8}Sr_{0.2}NiO_2$ superconductors. *Nat Commun* **13**, 743 (2022).

68. Wang, J. *et al.* Superconductivity in an Orbital-Reoriented SnAs Square Lattice: A Case Study of $Li_{0.6}Sn_2As_2$ and NaSnAs. *Angewandte Chemie International Edition* **62**, (2023).

69. Zhou, N. *et al.* Disorder-robust high-field superconducting phase of FeSe single crystals. *Phys Rev B* **104**, L140504 (2021).

70. Chow, L. E. *et al.* Pauli-limit violation in lanthanide infinite-layer nickelate superconductors. (2022).

71. Lee, Y. *et al.* Synthesis of superconducting freestanding infinite-layer nickelate heterostructures on the millimetre scale. *Nature Synthesis* (2025) doi:10.1038/s44160-024-00714-2.

72. Ekin, J. W. *Experimental Techniques for Low-Temperature Measurements*. (Oxford University Press, Oxford, UK, 2006).

73. Talantsev, E. F. & Tallon, J. L. Universal self-field critical current for thin-film superconductors. *Nat Commun* **6**, 7820 (2015).

74. Crump, W. P. & Talantsev, E. F. Software for fitting self-field critical current data. Preprint at (2016).

75. Gross-Alltag, F., Chandrasekhar, B. S., Einzel, D., Hirschfeld, P. J. & Andres, K. London field penetration in heavy fermion superconductors. *Zeitschrift fur Physik B Condensed Matter* **82**, 243–255 (1991).

76. Gross, F. *et al.* Anomalous temperature dependence of the magnetic field penetration depth in superconducting UBe13. *Zeitschrift fur Physik B Condensed Matter* **64**, 175–188 (1986).

77. Talantsev, E., Crump, W. P. & Tallon, J. L. Thermodynamic Parameters of Single- or Multi-Band Superconductors Derived from Self-Field Critical Currents. *Ann Phys* **529**, 1–18 (2017).

78. Talantsev, E. F., Crump, W. P. & Tallon, J. L. Universal scaling of the self-field critical current in superconductors: from sub-nanometre to millimetre size. *Sci Rep* **7**, 10010 (2017).

79. Prohammer, M. & Carbotte, J. P. London penetration depth of *d*-wave superconductors. *Phys Rev B* **43**, 5370–5374 (1991).

80. Talantsev, E. F. *et al.* p-wave superconductivity in iron-based superconductors. *Sci Rep* **9**, 14245 (2019).

81. Won, H. & Maki, K. *d*-wave superconductor as a model of high-T_c superconductors. *Phys Rev B* **49**, 1397–1402 (1994).

82. Bardeen, J., Cooper, L. N. & Schrieffer, J. R. Theory of Superconductivity. *Physical Review* **108**, 1175–1204 (1957).

83. Talantsev, E. F. *et al.* On the origin of critical temperature enhancement in atomically thin superconductors. *2d Mater* **4**, (2017).

84. Carrington, A. & Manzano, F. Magnetic penetration depth of MgB2. *Physica C Supercond* **385**, 205–214 (2003).

85.   Canfield, P. C., Bud'ko, S. L. & Finnemore, D. K. An overview of the basic physical properties of MgB2. *Physica C Supercond* **385**, 1–7 (2003).

86.   Buzea, C. & Yamashita, T. Review of the superconducting properties of MgB ₂. *Supercond Sci Technol* **14**, R115–R146 (2001).

87.   Talantsev, E. F. Solving mystery with the Meissner state in La3Ni2O7-δ. *Superconductivity: Fundamental and Applied Research* 65–76 (2024) doi:10.62539/2949-5644-2024-0-3-65-76.

88.   Talantsev, E. F., Mataira, R. C. & Crump, W. P. Classifying superconductivity in Moiré graphene superlattices. *Sci Rep* **10**, 212 (2020).

89.   Talantsev. Classifying Induced Superconductivity in Atomically Thin Dirac-Cone Materials. *Condens Matter* **4**, 83 (2019).

90.   Gumeniuk, R., Levytskyi, V., Kundys, B. & Leithe-Jasper, A. Yb3Rh4Sn13: Two-gap superconductor with a complex Fermi surface. *Phys Rev B* **108**, 214515 (2023).

91.   Wimbush, S. C. & Strickland, N. M. A Public Database of High-Temperature Superconductor Critical Current Data. *IEEE Transactions on Applied Superconductivity* **27**, 1–5 (2017).

92.   Lao, M. *et al.* High current variable temperature electrical characterization system for superconducting wires and tapes with continuous sample rotation in a split coil magnet. *Review of Scientific Instruments* **90**, (2019).

93.   Devitre, A. R. *et al.* A facility for cryogenic ion irradiation and *in situ* characterization of rare-earth barium copper oxide superconducting tapes. *Review of Scientific Instruments* **95**, (2024).

94.   Zhang, D. *et al.* Achieving superconductivity in infinite-layer nickelate thin films by aluminum sputtering deposition. (2024).

95.   Li, J. *et al.* Pressure-driven right-triangle shape superconductivity in bilayer nickelate La3Ni2O7. (2024).

96.   Wang, N. *et al.* Bulk high-temperature superconductivity in pressurized tetragonal La2PrNi2O7. *Nature* **634**, 579–584 (2024).

97.   Zhu, Y. *et al.* Superconductivity in pressurized trilayer La4Ni3O10-δ single crystals. *Nature* **631**, 531–536 (2024).

98.   Yan, X. *et al.* Superconductivity in an ultrathin multilayer nickelate. *Sci Adv* **11**, (2025).

99.   Chen, X. *et al.* Non-bulk Superconductivity in Pr4Ni3O10 Single Crystals Under Pressure. (2024).

100. Zhang, E. *et al.* Bulk superconductivity in pressurized trilayer nickelate Pr4Ni3O10 single crystals. (2025).

101. Storey, J. G. Incoherent superconductivity well above T_c in high-T_c cuprates—harmonizing the spectroscopic and thermodynamic data. *New J Phys* **19**, 073026 (2017).

102. Tallon, J. L., Storey, J. G. & Loram, J. W. Fluctuations and critical temperature reduction in cuprate superconductors. *Phys Rev B* **83**, 092502 (2011).

103. Stewart, G. R. Superconductivity in iron compounds. *Rev Mod Phys* **83**, 1589–1652 (2011).

104. Chiao, M. Are we there yet? *Nat Phys* **3**, 148–150 (2007).

105. Drozdov, A. P., Eremets, M. I., Troyan, I. A., Ksenofontov, V. & Shylin, S. I. Conventional superconductivity at 203 kelvin at high pressures in the sulfur hydride system. *Nature* **525**, 73–76 (2015).

106. Drozdov, A. P. *et al.* Superconductivity at 250 K in lanthanum hydride under high pressures. *Nature* **569**, 528–531 (2019).

107. Kong, P. *et al.* Superconductivity up to 243 K in the yttrium-hydrogen system under high pressure. *Nat Commun* **12**, 5075 (2021).

108. Somayazulu, M. *et al.* Evidence for Superconductivity above 260 K in Lanthanum Superhydride at Megabar Pressures. *Phys Rev Lett* **122**, 027001 (2019).

109. Bhattacharyya, P. *et al.* Imaging the Meissner effect in hydride superconductors using quantum sensors. *Nature* **627**, 73–79 (2024).

110. Troyan, I. A. *et al.* Anomalous High-Temperature Superconductivity in YH6. *Advanced Materials* **33**, 2006832 (2021).

111. Semenok, D. Computational design of new superconducting materials and their targeted experimental synthesis. *PhD Thesis; Skolkovo Institute of Science and Technology* (2023) doi:10.13140/RG.2.2.28212.12161.

112. Minkov, V. S., Ksenofontov, V., Bud'ko, S. L., Talantsev, E. F. & Eremets, M. I. Magnetic flux trapping in hydrogen-rich high-temperature superconductors. *Nat Phys* **19**, 1293–1300 (2023).

113. Minkov, V. S. *et al.* Revaluation of the lower critical field in superconducting H$_3$S and LaH$_{10}$ (Nature Comm. 13, 3194, 2022). (2024).

114. Minkov, V. S. *et al.* Magnetic field screening in hydrogen-rich high-temperature superconductors. *Nat Commun* **13**, 3194 (2022).

115. Tallon, J. L. & Talantsev, E. F. Compressed H3S, superfluid density and the quest for room-temperature superconductivity. *J Supercond Nov Magn* **31**, 619–624 (2018).